5-2020

Computational Simulations of Temperature-Dependent Dynamics in Type II Superconductors Using a Material Specific Formulation of Ginzburg Landau Theory

Aiden Harbick

Computational Simulations of Temperature-Dependent Dynamics in Type II Superconductors Using a Material Specific Formulation of Ginzburg Landau Theory

A thesis submitted in partial fulfillment of the requirement
for the degree of Bachelor of Science with Honors in
Physics from the College of William and Mary in Virginia,

by

Aiden V. Harbick

Accepted for Honors

George Vahala

Prof. George Vahala, Advisor

Keith Griffioen

Prof. Keith Griffioen

Richard Marcus

Prof. Richard Marcus

Williamsburg, Virginia
May 8 2020

Computational Simulations of Temperature-Dependent Dynamics in Type II Superconductors Using a Material Specific Formulation of Ginzburg Landau Theory

A thesis submitted in partial fulfillment of the requirement
for the degree of Bachelor of Science with Honors in
Physics from the College of William and Mary in Virginia,

by

Aiden V. Harbick

Accepted for Honors

Prof. George Vahala, Advisor

Prof. Keith Griffioen

Prof. Richard Marcus

Williamsburg, Virginia
May 8 2020

Contents

Acknowledgments

I would like to thank my mentor, Dr. Mark Transtrum, for his guidance in exploring this challenging topic. I also thank Alden Pack, Cole Abbot, Braedon Jones, Jared Carlson, Danilo Liarte, and Sam Posen for many helpful discussions. Additionally, I thank Dr. George Vahala and Dr. Keith Griffioen for their help in revising this thesis as well as navigating the W&M honors process. Finally, I would like to thank my parents, Andrew and Shiree Harbick, for their love and support in all my personal and academic endeavors and without whom I would not be where I am now.

List of Figures

List of Tables

Abstract

Superconducting Radio Frequency (SRF) cavities play a fundamental role in particle accelerators. Efficient operation depends on expelling magnetic flux from the cavity, and any residual flux that remains trapped after cooling below the critical temperature can have a significant impact on performance. Experimental evidence suggests that material defects as well as cooling protocols can have a strong impact on subsequent performance. To better understand these phenomena, we use time-dependent Ginzburg-Landau theory implemented as finite-element simulations. We adapt the theory to allow spatial variation of material-specific parameters along with realistic temperature dependencies. We report on numerical experiments for different configurations of defects such as pinning sites and grain boundaries, finding that grain boundaries have a much larger effect than pinning sites on the ability of a superconductor to expel magnetic flux. We also report on numerical experiments where we investigated effects of cooling speeds on magnetic flux expulsion, observing qualitative changes which occur when we change a parameter which controls the time dynamics of our simulations. We discuss implications for SRF cavity design and operation as well as future research.

Chapter 1

Introduction

Accelerated particle beams have a variety of applications for imaging in the engineering and natural sciences. Biologists use x-ray beams for imaging proteins [1], engineers use them to develop new semiconductor technologies [2], and physicists use them to study magnetic materials [3]. These applications all need bright, coherent, tunable beams, however the size and cost of the accelerators used to produce these beams is prohibitive to many of these applications.

The first particle accelerators were initially built in the early 1930s, though these accelerators were rather primitive by today's standards. Modern particle accelerators really developed in the 1960s and 1970s after the Stanford Linear Accelerator Center (SLAC) was funded and built by the US federal government. The accelerators built at SLAC were some of the first to incorporate superconductors which massively boosted their power output [4]. Today, particle accelerator experiments are some of the largest and most expensive scientific operations, so there is a large push in the scientific accelerator community to improve the size and efficiency of particle beam acceleration to make this incredible technology available to even more scientists.

There are many different factors that go into the creation of particle beams, but the focus of this project is on particle acceleration. Beam acceleration is often handled by superconducting radio frequency (SRF) cavities [5]. These cavities work by being supplied an AC current, which then induces internal electromagnetic fields, which can then be tuned to accelerate clusters of electrons or other particles as they pass through the center of the

cavities. Figure 1.1 depicts a single SRF cavity; a synchrotron (a type of large particle accelerator) may have up to hundreds of these cavities in series. The cavities are plated with Niobium and cooled to around 2 Kelvin so that the Niobium enters a superconducting state, and the superconducting state results in a very small, but non-negligible, AC resistance. This allows for the largest and highest frequency electromagnetic fields to be induced, thus creating the brightest beams. Niobium has a critical temperature of around 9 Kelvin. Some cavities are made of Nb_3Sn, which has a critical temperature of 18 Kelvin [6]. If it were possible to raise the operating temperature of SRF cavities by improving their stability, they would require fewer cryogenic facilities and their size and maintenance cost would decrease. One of the main goals of current research efforts is to explore some of the limiting factors to SRF cavity stability and performance.

Building and testing SRF cavities is a difficult endeavor. Purchasing and maintaining all the components of an SRF cavity is currently very expensive, and actually measuring the physics behind dynamic superconductivity is challenging. As such, numerical simulations of SRF cavities are incredibly useful for getting an idea of what will happen experimentally. The predictions of SRF cavity simulations can then be used to guide development efforts [7].

1.1 Superconductivity and Ginzburg-Landau Theory

The phenomenon of superconductivity was first discovered by Kamerlingh Onnes in 1911 [8]. A material which has entered the superconducting state has two key properties at a macroscopic level: negligible DC resistance (and small but non-negligible AC resistance) and perfect diamagnetism, i.e., the expulsion of magnetic fields, known as the Meissner effect. The Meissner effect occurs when surface currents in the superconducting material form and cancel out any external magnetic field. The material exits the superconducting state if it goes above some critical temperature, or if there are external fields that are strong enough to break through the Meissner effect. This work largely focuses on macroscopic effects of the superconducting state, for more information on microscopic effects and the superconducting phenomenon in general, see [9]. For SRF cavities, small AC resistance is

Figure 1.1: A picture of an SRF cavity. Courtesy of Sam Posen from Fermilab. There are coils above and below the cavity to control the magnetic field applied on the cavity. When used for acceleration, an AC current is run through the torroidal region, and the particles are accelerated by induced electromagnetic fields as they pass through the middle of the cavity

a desirable property, whereas the loss of superconductivity due to the breakdown of the Meissner effect is a limitation.

There are many potential models for superconductivity that we could choose to use in order to simulate SRF cavities [10]. Our research uses the Ginzburg-Landau equations because they capture the macroscopic features we are interested in such as the difference between type I and type II superconductors and vortex dynamics. These equations also are valid for large variations in the magnetic field, unlike other similar models that also capture macroscopic features. There is a large body of work deriving the Ginzburg-Landau equations; however, doing so here is beyond the scope of this thesis, for this the curious

reader should refer to [11]. The particular equations we are using for this project are the time-dependent Ginzburg-Landau (TDGL) equations in dimensionless units:

$$\frac{\partial \psi}{\partial t} + i\kappa\theta\psi + \left(\frac{-i}{\kappa}\nabla + \mathbf{A}\right)^2 \psi - \psi + |\psi|^2\psi = 0 \text{ in } \Omega, \tag{1.1.1}$$

$$\frac{1}{u}\left(\frac{\partial \mathbf{A}}{\partial t} - \nabla\theta\right) + \nabla \times \nabla \times \mathbf{A} + \frac{i}{2\kappa}\left(\psi^*\nabla\psi - \psi\nabla\psi^*\right) + |\psi|^2\mathbf{A} = \nabla \times \mathbf{H} \text{ in } \Omega, \tag{1.1.2}$$

$$\left(\frac{i}{\kappa}\nabla + A\right) \cdot n = \mathbf{H} \times n \text{ on } \Gamma, \tag{1.1.3}$$

$$(\nabla \times A) \times n = \mathbf{H} \times n \text{ on } \Gamma, \tag{1.1.4}$$

$$\mathbf{E} \cdot n = 0 \text{ on } \Gamma, \tag{1.1.5}$$

where $\mathbf{A}$ is the magnetic vector potential, ψ is a complex order parameter which has units such that its norm represents the fraction of available electrons in the superconducting state. This means it is a normal metal when $|\psi|^2 = 0$ and is perfectly superconducting when $|\psi|^2 = 1$. $\mathbf{H}$ is the applied magnetic field. Ω is the superconducting region, and the boundary of the region is Γ. κ is a dimensionless constant which represents the ratio of the penetration depth and the coherence length. The penetration depth (also known as the London penetration depth) is the characteristic length scale for the decay of the magnetic field within the superconducting material, and the coherence length is the characteristic length scale for variations in the order parameter. n is a vector normal to Γ. θ is the electric potential, $\mathbf{E} = -\nabla\theta - \frac{\partial \mathbf{A}}{\partial t}$ is the electric field. It should be noted that the gauge choice for the equations here is such that $-\theta = \nabla \cdot \mathbf{A}$, this will be relevant later. u is similar to κ, except that while κ is a ratio of characteristic length scales, u is a ratio of time scales: the characteristic response time of ψ and the characteristic response time of $\mathbf{A}$. Changing u affects the way in which time dynamics occur within the superconductor and as such it is typically set to 1, though as we will see in Chapter 3, changing it has some pretty meaningful implications. Equation 1.1.1 controls the solution for ψ. Note how it bears many similarities to the Schrodinger equation, with the exception of the final term with a nonlinear $|\psi|^2\psi$. Equation 1.1.2 controls the solution for $\mathbf{A}$ primarily, as well as other important electromagnetic quantities, note how the $\nabla \times \nabla \times \mathbf{A}$ term is a current.

The solutions to these equations can then be used to analyze the superconductivity of the material in the given region under the given initial conditions. It should be noted that the above equations are dimensionless; appendix A shows how the nondimensionalization process works.

The superconductors used in SRF cavities are type II superconductors. In GL theory, type I superconductors have $\kappa < \frac{1}{\sqrt{2}}$ whereas type II superconductors have $\kappa > \frac{1}{\sqrt{2}}$. The key difference between type I and II superconductors is that type II have 2 critical magnetic fields, and an extra phase called the mixed state in which the nucleation of Abrikosov vortices occurs rather than a complete quenching of the Meissner state. A phase diagram for types of superconductors is shown in figure 1.2 [7].

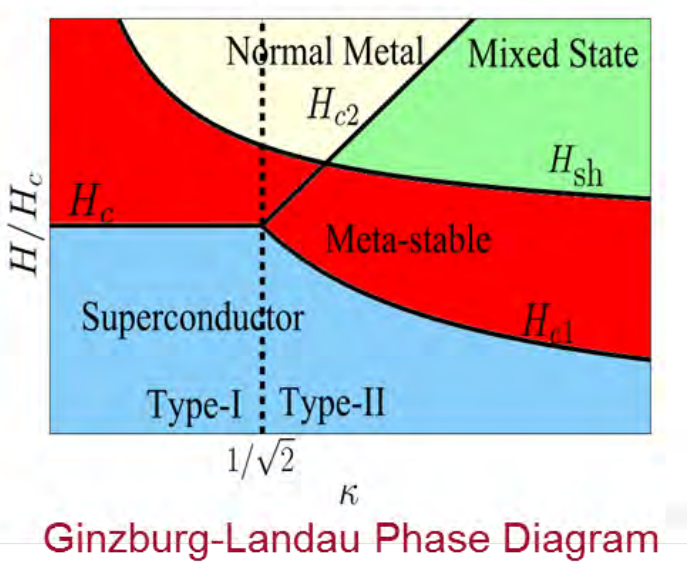

Figure 1.2: A phase diagram for different phases of superconductors at a temperature below the critical temperature, The x axis is κ and the y axis is the applied field. The meta-stable state is a state where the material is at risk of losing superconductivity, but an energy barrier is preventing it from doing so, the super-heating field, H_{sh}, is the field at which there is enough energy for the transition to either normal metal or mixed state to occur

1.2 Objective

When an SRF cavitiy is prepared, it is first demagnetized, such that the only magnetic fields existing in it is Earth's magnetic field and some other small residual fields. The SRF cavity

is then cooled by pumping liquid helium through reservoirs surrounding it until it reaches the superconducting phase, and the Meissner effect can push out remaining magnetic fields. In practice, the magnetic field is not perfectly expelled from the cavities, and some magnetic field may become trapped in spots called pinning sites, which are due to material defects or impurities [12]. Intuitively, it may seem like slowly cooling the SRF cavity by gradually pumping the liquid helium through the reservoirs would allow the material more time to push out the magnetic field as the material is cooled in a 'wave', however it turns out that experimentally, the performance of SRF cavities is actually better when the helium is quickly blasted through the reservoirs; there is not currently a good theoretical explanation for why this results in better magnetic flux expulsion. Posen et al. have also determined that cavity preparation, which can have an effect on the number and types of pinning sites within an SRF cavity, has large effects on the magnetic flux expulsion as well [13].

The goal of this project is to simulate what happens to different superconductors as they are cooled, and how these results are affected by different material defects. The results of such simulations should be able to spur some insights into why the above phenomena occur, as well as providing some guidance for the direction of future experimental and computational work. In order to achieve this, we needed to re-factorize existing simulations to consider time and space varying temperature, as well as to solve the equations with multiple different materials within the same domain.

1.3 Overview of this Thesis

In Chapter 2 we discuss more of the theory behind our simulations, in particular we discuss the formulation of the TDGL equations which we have developed to simulate domains with spatially and temporally varying material parameters.

In Chapter 3 we go over the results of the many simulations we ran throughout the course of this project. Broadly speaking there are 6 categories of simulations we ran: pushing vortices with temperature waves, pushing vortices into pinning sites with temperature waves, pushing vortices into grain boundaries with temperature waves, testing pinning site vortex

nucleation ability, testing grain boundary vortex nucleation ability, and investigating the effects of varying u_0 (a parameter we define in Chapter 2).

In Chapter 4 we summarize the key takeaways from our simulations and make some recommendations for future simulations and research questions.

Chapter 2

Numerical Formulations

To actually solve the time-dependent GL equations we use a finite element method (FEM). FEMs work by discretizing a particular domain of interest into many smaller domains (finite elements), approximating a solution on that finite element, and then putting the solutions for each finite element together to get an approximation for the whole unknown function. We use an open source Python library for solving partial differential equations via finite element called FEniCS. For more info on FEniCS and FEMs, visit https://fenicsproject.org and refer to [14].

2.1 Single Material Formulation

There are a number of different ways that the TDGL equations can be formulated for FEMs. We start by using a particular method proposed by Gao which lets us solve them in 2D [15]. We have chosen to do this because the Ginzburg-Landau simulations are quite computationally expensive, and 2D simulations can already take many hours to run. 3D simulations of similar phenomena can take between 2 and 4 orders of magnitude longer than 2D simulations to run, which would severely limit the number of simulations we could do. 2D simulations are very useful for understanding qualitative behaviors of superconductors, which can be later checked in 3D if the need arises. Under Gao's formulation, we let $\theta = -\nabla \cdot \mathbf{A}$ (The TDGL equations are gauge invariant [16], so we can choose our gauge such that this is the case) and $\sigma = \nabla \times \mathbf{A}$. σ and $\mathbf{H}$ are the internal and applied magnetic fields respectively and in principle can be in any direction, however, since in 2D $\mathbf{A}$ is only in the $x - y$ plane,

σ will always be in the z direction only, so we can just represent it as its magnitude, which is a scalar function. As such, we also chose to define $\mathbf{H}$ to be only in the z direction as well, and we implement it as a scalar function H. With this in mind, we can get two new equations by taking the curl and divergence of equation 1.1.2. Interestingly, Gao has found that formulating the equations in this way, with two additional equations to solve ends up being faster and more stable using a FEM, as previous solutions for σ and θ can be used to find future timestep solutions of $\mathbf{A}$. The full equations which we solve are:

$$\frac{\partial \psi}{\partial t} - i\kappa\theta\psi + \left(\frac{i}{\kappa}\nabla + \mathbf{A}\right)^2 \psi - \psi + |\psi|^2\psi = 0, \tag{2.1.1}$$

$$\frac{1}{u}\left(\frac{\partial \mathbf{A}}{\partial t} - \nabla\theta\right) + \nabla \times \sigma + \frac{i}{2\kappa}\left(\psi^*\nabla\psi - \psi\nabla\psi^*\right) + |\psi|^2\mathbf{A} = \nabla \times H, \tag{2.1.2}$$

$$\frac{1}{u}\frac{\partial \sigma}{\partial t} - \nabla^2\sigma + \frac{i}{2\kappa}\nabla \times \left(\psi^*\nabla\psi - \psi\nabla\psi^*\right) + |\psi|^2\sigma - \mathbf{A} \cdot \nabla \times |\psi|^2 = -\nabla^2 H, \tag{2.1.3}$$

$$\text{and } \frac{1}{u}\left(\frac{\partial \theta}{\partial t} - \nabla^2\theta\right) + \frac{i}{2\kappa}\nabla \cdot \left(\psi^*\nabla\psi - \psi\nabla\psi^*\right) + |\psi|^2\theta + \mathbf{A} \cdot \nabla|\psi|^2 = 0, \tag{2.1.4}$$

with boundary conditions

$$\left(\frac{i}{\kappa}\nabla\psi + \mathbf{A}\psi\right) \cdot n = 0, \qquad \sigma = H, \qquad \text{and } \frac{\partial \theta}{\partial n} = 0. \tag{2.1.5}$$

Solving these equations with FEniCS allows us to simulate the superconductor dynamics of a single material; however, in order to simulate SRF cavity cooling, we required the ability to simulate different materials at varying temperatures. The above formulation of the TDGL equations assumed that the material coefficients remain the same in the domain, and said coefficients were then set to 1. To change this, we had to revisit the nondimensionalization of the TDGL equations and allow certain material coefficients to vary with time and space.

2.2 Variable Material Formulation

The GL equations (excluding the boundary conditions) look like this before we nondimensionalize them:

$$\Gamma\left(\frac{\partial \psi}{\partial t} + \frac{ie_s\theta}{\hbar}\psi\right) + \frac{1}{2m_s}\left(-i\hbar\nabla - \frac{e_s}{c}\mathbf{A}\right)^2 \psi + \alpha\psi + \beta|\psi|^2\psi = 0 \text{ and} \tag{2.2.1}$$

$$\frac{4\pi\sigma_n}{c}\left(\frac{1}{c}\frac{\partial \mathbf{A}}{\partial t}+\nabla\theta\right)+\nabla\times\nabla\times\mathbf{A}-\frac{2\pi i e_s\hbar}{m_s c}\left(\psi^*\nabla\psi-\psi\nabla\psi^*\right)-\frac{4\pi e_s^2}{m_s c^2}|\psi|^2\mathbf{A}=0, \quad (2.2.2)$$

where c is the speed of light, e_s is the charge of a Cooper pair (or twice the charge of an electron), and m_s is the mass of a Cooper pair. α and β are simply scalar coefficients that are functions of the penetration depth, the critical field, the critical temperature, and temperature. Γ is a constant scaling factor on the time relaxation rate of ψ, and σ_n is the electrical conductivity [17]. To nondimensionalize these equations we follow the processes outlined by Du [11] and Kopnin [17], but instead of entirely nondimensionalizing α, β, and Γ out of the equations, we set each of these coefficients to the product of some reference value which has units and a unitless function of time and space, i.e. $\alpha = \alpha_0 a(\mathbf{r},t)$, $\beta = \beta_0 b(\mathbf{r},t)$, and $\Gamma = \Gamma_0\gamma(\mathbf{r},t)$. Making these assumptions and proceeding with the nondimensionalization as normal, we get the following equations:

$$\gamma\left(\frac{\partial\psi}{\partial t}-i\kappa_0\theta\psi\right)+\left(\frac{i}{\kappa_0}\nabla+\mathbf{A}\right)^2\psi-a\psi+b|\psi|^2\psi=0, \quad (2.2.3)$$

$$\frac{1}{u_0}\left(\frac{\partial\mathbf{A}}{\partial t}-\nabla\theta\right)+\nabla\times\sigma+\frac{i}{2\kappa_0}\left(\psi^*\nabla\psi-\psi\nabla\psi^*\right)+|\psi|^2\mathbf{A}=\nabla\times H, \quad (2.2.4)$$

$$\frac{1}{u_0}\frac{\partial\sigma}{\partial t}-\nabla^2\sigma+\frac{i}{2\kappa_0}\nabla\times\left(\psi^*\nabla\psi-\psi\nabla\psi^*\right)+|\psi|^2\sigma-\mathbf{A}\cdot\nabla\times|\psi|^2=-\nabla^2 H, \quad (2.2.5)$$

$$\text{and } \frac{1}{u_0}\left(\frac{\partial\theta}{\partial t}-\nabla^2\theta\right)+\frac{i}{2\kappa_0}\nabla\cdot\left(\psi^*\nabla\psi-\psi\nabla\psi^*\right)+|\psi|^2\theta+\mathbf{A}\cdot\nabla|\psi|^2=0. \quad (2.2.6)$$

The derivation of this result is rather long and not enormously important to understanding the rest of this thesis; however, the curious reader can refer to Appendix A for the full derivation. This is the formulation we will be utilizing from this point on. It should be noted that the only real differences between these equations and the single material formulation from Section 2.1 is the addition of a, b, and γ (which are functions of $\mathbf{r}$ and t) in front of several of the terms in Equation 2.1.1 and κ and u have now become κ_0 and u_0. The reason for these subscripts is because it can be shown that κ and u depend on β and Γ respectively. κ and u are defined so that they necessarily must be constants, so letting $\beta = \beta_0 b(\mathbf{r},t)$ and $\Gamma = \Gamma_0\gamma(\mathbf{r},t)$ means κ and u are no longer necessarily constant, so we instead define κ_0 and

u_0, which depend on β_0 and Γ_0 respectively. If b and γ are chosen to be constants as well, then $\kappa = \kappa_0$ and $u = u_0$. If b and γ are not constant, there is an effective κ and u which varies along with b and γ; κ_0 and u_0 determine what this effective value is when b and γ are 1.

2.3 Specifying Materials

To solve the TDGL equations, we then just need to provide values for a, b, and γ. a and b are not inherent material parameters, but they do depend on real material parameters as well as the temperature such that

$$a(H_c, \lambda, T_c, T) = H_c^2 \lambda^2 \frac{1 - \left(\frac{T}{T_c}\right)^2}{1 + \left(\frac{T}{T_c}\right)^2} \tag{2.3.1}$$

$$\text{and } b(H_c, \lambda, T_c, T) = H_c^2 \lambda^4 \frac{1}{\left(1 + \left(\frac{T}{T_c}\right)^2\right)^2}, \tag{2.3.2}$$

where H_c is the critical magnetic field, λ is the London penetration depth, T_c is the critical temperature, and T is the temperature. Note that when a is positive, the material is superconducting, and is a normal metal when a is negative. With these formulas, all we have to do is specify H_c, λ, T_c, and T and our code will generate a and b as seen in Figure 2.1. Varying the temperature profile over the domain will modify our a plot to reflect this, as shown by Figure 2.2. Giving the temperature a time dependence is how we simulate cooling processes. It should be noted that in our simulations, we assume we have full control over the temperature, and do not take into account any small effects that various superconductor dynamics have on the temperature. From here it is a simple matter of submitting a job to a supercomputer to find a finite element solution for ψ, $\mathbf{A}$, σ, and θ at each time step, and then plotting observable values from these solutions. The code used in running our simulations can be found at https://git.physics.byu.edu/rfsc/tdgl.

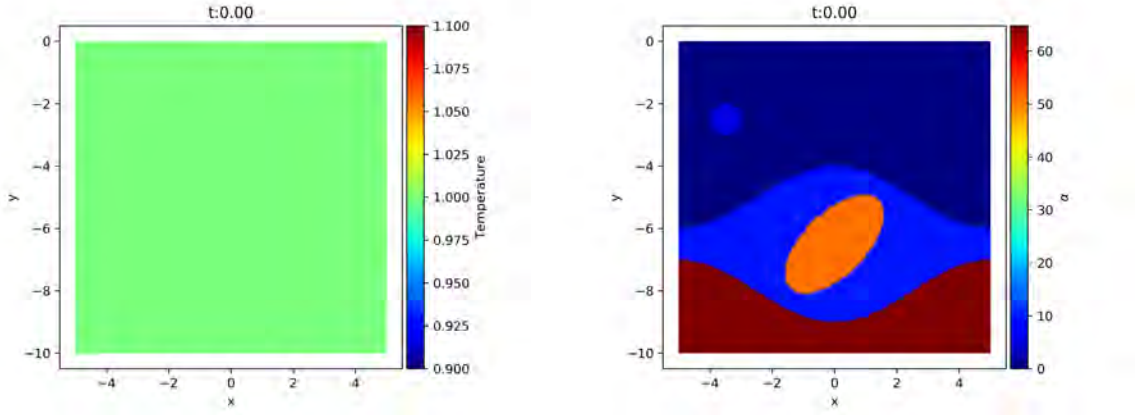

(a) Temperature profile (b) Plot of a under this temperature profile

Figure 2.1: Plots of temperature and a within a 10x10 domain at this temperature. The temperature is shown in (a). In (b), each region (or in this case, color) represents a different material with different H_c, λ, and T_c, the value is then calculated with Equation 2.3.1. The values in this particular graph were chosen arbitrarily, so disregard the specific values of a, this just shows what a multi-material domain could look like. There are two main structures we can input: layers, which are the larger regions separated by a boundary, and islands which are the ellipses. Small islands can be used as pinning sites.

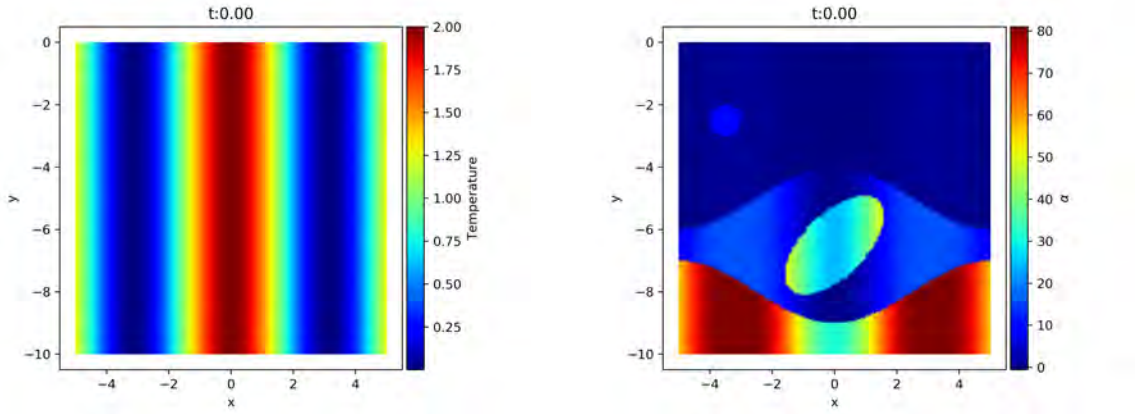

(a) Temperature profile (b) Plot of a under this temperature profile

Figure 2.2: A plot of a temperature profile and a under this profile within a 10x10 domain for this temperature profile. The H_c, λ, and T_c are the same as they are in Figure 2.1, but now the sinusoidal temperature dependence shown in (a) is altering the value of a, shown in (b), within any given region of the material.

2.4 Simulation Unit Conversions

The simulations in this thesis are mostly intended to be treated qualitatively, allowing us to explore relevant phenomena while keeping simple numerical values for non-relevant pa-

rameters, however it should certainly be documented that our code is capable of using very specific material values if they are known, and these values can be converted to and from simulation units. Since everything in the simulation is dimensionless, every variable is scaled in some way (the details of which can be found in appendix A); however, in particular it is interesting to discuss the scaling of position and time. The spatial dimensions are scaled by the penetration depth λ_0 such that $x \to \lambda_0 x$ and $y \to \lambda_0 y$. This means that in our simulation a 10x10 domain is actually a $10\lambda_0$x$10\lambda_0$ domain. Table 2.1 shows some common spatial material parameters for materials used in SRF cavities. Here we see that the penetration depth for Niobium is 50 nm, which means a 10x10 simulation would correspond to an area of $0.25\mu\text{m}^2$. Similarly, time is scaled by $t \to \tau_\Delta t$ where τ_Δ is the characteristic timescale of the order parameter; this means a time of 10 in simulation units is actually $10\tau_\Delta$ seconds in real time. There is significantly less documentation of values for the characteristic timescales of TDGL theory; however, Oripov [18] calculates that for Niobium at least, τ_Δ is on the order of 10^{-12} seconds, which means the time dynamics we are looking at are actually quite fast.

Material	$\lambda(T=0)$ [nm]	$\xi(T=0)$ [nm]	$\mu_0 H_{sh}$ [mT]	T_c [K]
Nb	50	22	219	9.2
Nb_3Sn	111	4.2	425	18
MgB_2	185	4.9	170	37
NbN	375	2.9	214	16

Table 2.1: Table of material parameters for superconductors used in SRF cavities. λ is the London penetration depth, ξ is the coherence length, H_{sh} is the superheating field, and T_c is the critical temperature. These values were taken from [6].

Chapter 3

Numerical Simulation Results

This chapter contains plots and diagrams of the many simulations we ran over the course of this project. There is a lot of information to process in these plots, but there are a few things which are particularly important to keep in mind. Firstly, when solving the TDGL equations, we have to provide an applied magnetic field, H_a. Since we are solving the equations in 2D, all magnetic field is in the z direction and H_a is applied along the top and bottom edges of the domain. Our domains are periodic in the x direction. Because of this we often use periodic functions as our temperature profiles, since we can simulate cooling fronts travelling as far as necessary by simply translating the temperature profile in time; we use triangle waves most commonly because of their linear temperature gradients. Additionally, all of these simulations have $\kappa_0 = 4$. This is of course a parameter we could change, however, it controls the length scales in the simulation and we are more interested in time-dependent dynamics so we have left κ_0 constant through all of our simulations.

3.1 Temperature Profile

The function which we choose to use as temperature is important as it is the primary method by which we will simulate superconductor cooling. The function we have chosen to use throughout this thesis is given by

$$T(x, y, t) = \frac{2}{\pi} \arcsin\left(\cos\left(\pi\left(\frac{x}{25} + v(t - t_0)\right)\right)\right) + 1, \tag{3.1.1}$$

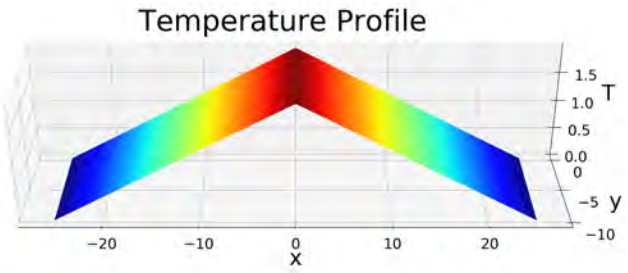

(a)

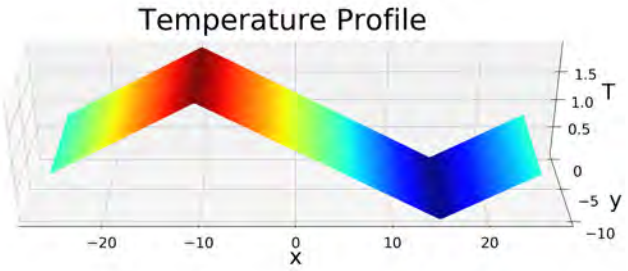

(b)

Figure 3.1: A plot of the temperature profile used in the rest of this thesis. The function here is given by Equation 3.1.1. Note that this function is periodic in x, as is necessarily the case since our domain is periodic in x. (a) shows the wave for $t = 0$. The temperature reaches a value of 2 at $x = 0$ and is 0 at $x = \pm 25$. (b) shows the wave after it has moved a short distance after some time t at a velocity v.

where v is the speed of the wave (if we want it to be moving) and t_0 is the starting time of the simulation run. A plot of this function for $t = 0$, $t_0 = 0$ is shown in Figure 3.1 (a). We wanted to choose a function which is periodic, as our domain is periodic in x, and this gives us the advantage of being able to move the wave for as long as desired, not being bounded by a finite domain. We have chosen this periodic function in particular because, as a triangle wave, it has linear temperature gradients and so we do not need to worry about effects due to changes in the slope of the temperature function in something like a sine or cosine. Figure 3.1 (b) shows the same wave after a brief time moving at a $v > 0$. The wave has simply translated to the left, given that it is a periodic function, the edge of another wave appears to the right. The direction it moves is arbitrary, but we have chosen to use left moving waves throughout this thesis.

3.2 Two Key Stationary Solutions

There are two situations in which we are particularly interested in looking at the effect of material defects on superconductor magnetic flux expulsion: situations in which existing vortices encounter a defect as they are being pushed out of the superconductor, and situations where new vortices may be formed because of said pinning sites. In order to simulate these two cases, we simply find a steady state solution for a non-moving temperature wave which has vortices and one which does not, and then we use these solutions as initial conditions for simulations with a moving temperature wave.

Figure 3.2 shows the steady state solution which contains vortices. The material parameters here are all constant throughout the domain with $H_c, \lambda, \gamma = 1$ and $T_c = 1.5$. We chose this T_c simply because it means more of the domain will be superconducting since our temperature varies between 0 and 2, and the most interesting dynamics happen in the superconducting or mixed states. The steady state depicted in plot (d) is notable for several reasons. Firstly, we are able to see all three different states of a superconductor: normal metal, mixed state, and superconducting. Plots of $|\psi|^2$ show information about the superconductivity. When $|\psi|^2 = 0$, the material is in the normal metal state, when $|\psi|^2 = 1$ the material is perfectly superconducting, and when $0 < |\psi|^2 < 1$ the material is imperfectly superconducting. a (calculated from Equation 2.3.1) and H_a are what primarily determine whether a material will be in the mixed state. If H_a is too low, no vortex will be able to nucleate and there will be no mixed state. When H_a gets large enough, vortices will be able to enter the superconductor and there will be a mixed state. a controls where this threshold is; when a is higher, H_a must be higher, and similarly a lower a means H_a can be lower. When $a < 0$, it means the material is unable to superconduct, and therefore also cannot enter the mixed state either. For these steady state solutions we are using constant material parameters, so the only thing causing a to vary is the temperature. $a = 0$ when $T = 1.5$, and the H_a of 0.2 is able to create a mixed state up until about $T = 1$, where $a = 0.36$. Increasing H_a would allow the vortices to penetrate further into the superconducting region,

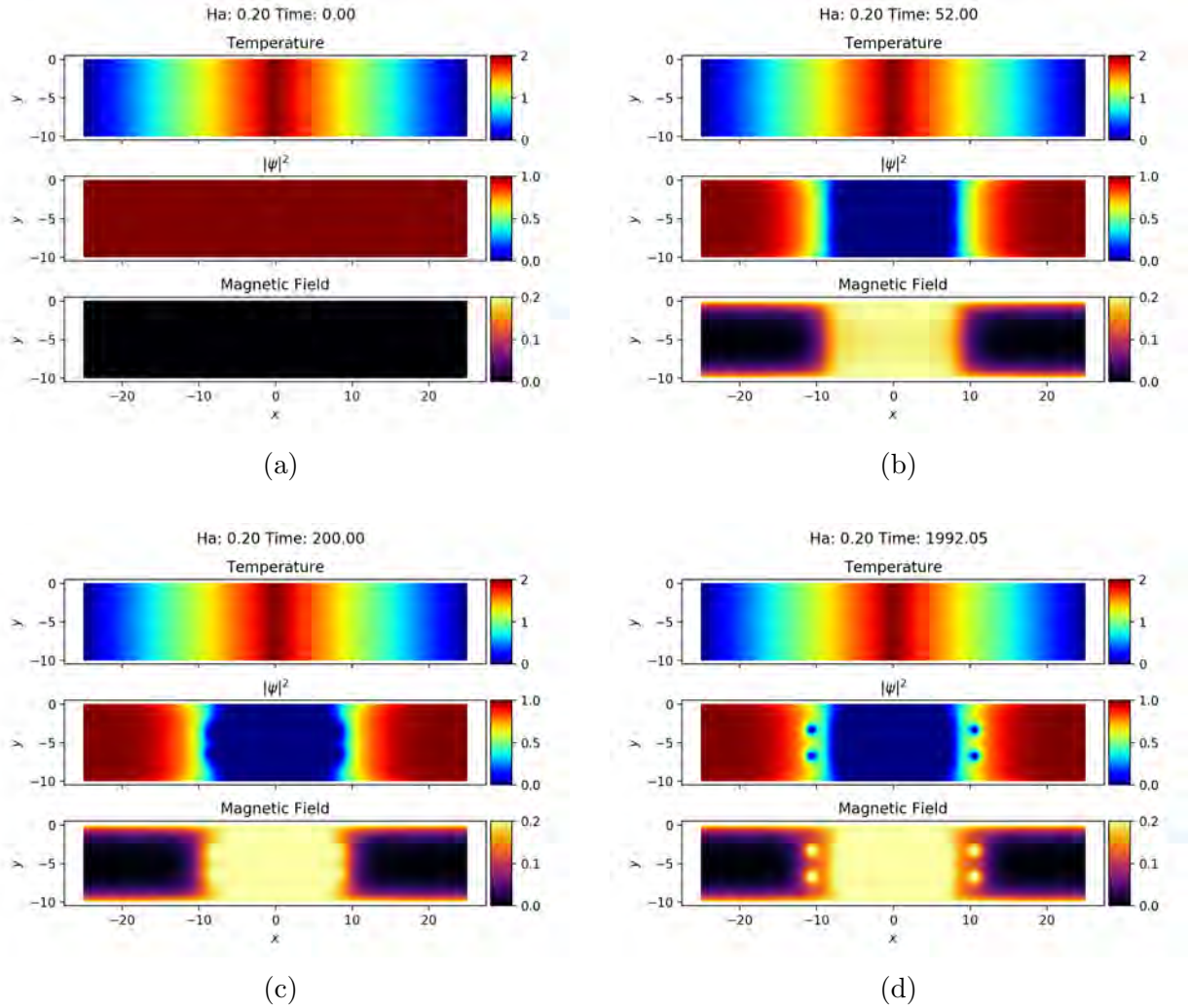

Figure 3.2: A steady state solution with vortices. For each subplot, the top plots show the temperature profile, which is given by Equation 3.1.1 with $v = 0$, the middle plots show $|\psi|^2$, and the bottom plots show the magnetic field magnitude. Above all the subplots is shown the applied magnetic field magnitude and the time of the simulation. There is only one material in this simulation with material coefficients $H_c, \lambda, \gamma = 1$ and $T_c = 1.5$. In (a), we start with initial conditions of $|\psi|^2 = 1$ and the magnetic field $\sigma = 0$. After a short time, shown in (b), the middle of the domain where the temperature is above T_c enters the normal state. In (c), some vortices have begun to enter the domain, and by (d) they have fully entered. The $|\psi|^2$ plot in (d) shows there are three different material states in this simulation: the blue region is the normal state, the red regions are the superconducting states, and the mixed states are between these two where there are color gradients. Note that the mixed states first begin where the temperature drops just below T_c. Two vortices have nucleated in each mixed state, and the magnetic field plot shows that magnetic field is penetrating the material in the location of each vortex.

whereas decreasing it would push them back towards the normal metal region.

Figure 3.3 shows our steady state solution with no vortices. As we mentioned, a lower

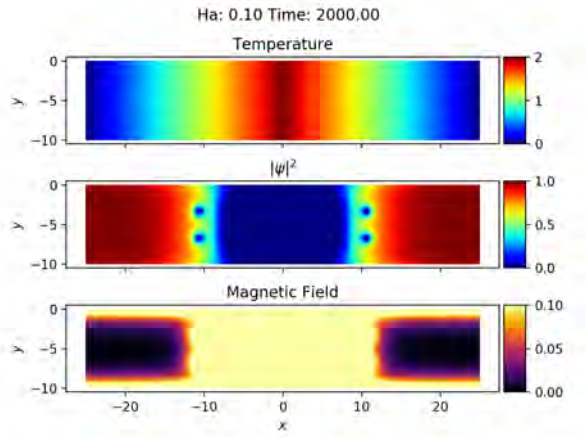

(a)

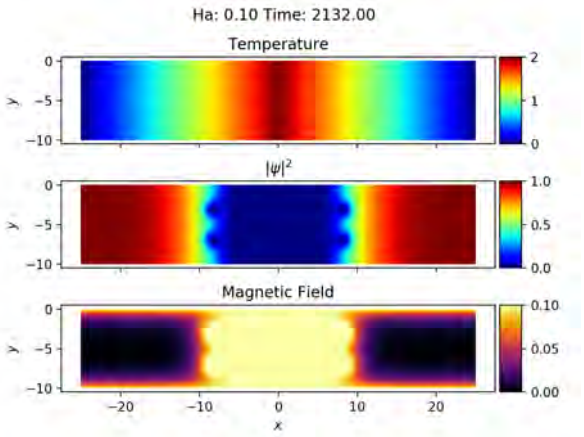

(b)

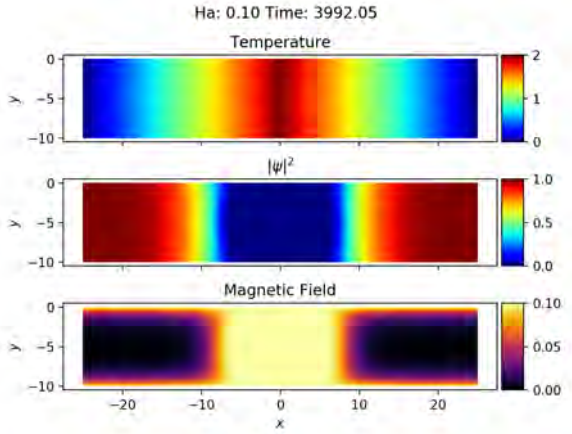

(c)

Figure 3.3: A steady state solution with no vortices. In (a) we start with the solution from Figure 3.2 as our initial condition. The difference is we have lowered H_a from 0.2 to 0.1 and so the vortices begin to be pushed out in (b) and are fully pushed out and the system again reaches a steady state but with no vortices at (c).

applied field may not allow vortices to enter the superconducting region, and so to get this solution we simply used our steady state solution which contains vortices, and lowered the applied magnetic field so that the vortices are no longer able to stably remain in a mixed state.

3.3 Pushing Vortices

While a vortex can be pushed into a superconducting region by a sufficiently high H_a, it also feels effective 'forces' due to temperature gradients and from being pushed out by stronger

superconducting regions [19]. When the temperature wave is then moved, the force from both the superconducting region and the temperature gradient cause the vortices to be pushed along, a behavior seen in Figure 3.4. Again, the function we use for a moving triangle wave is given by Equation 3.1.1 and is depicted in Figure 3.1. To push vortices, we simply use the steady state solution we found in Figure 3.2 as initial conditions for our simulation, and then we move the temperature wave at some velocity. When we refer to a velocity from this point on we are referring to the velocity v in Equation 3.1.1 unless otherwise specified.

Moving the wave in Figure 3.4 25% faster results in another interesting behavior, as shown in Figure 3.5. In this simulation, the temperature wave moves faster than the vortex is able to move, and it instead lags behind the portion of $|\psi|^2$ which has a steep slope and gets stuck in the superconducting region instead. This is a promising result, as our objective is to investigate cases in which changing the way cooling occurs changes the resulting amount of vortices left in the material. Here, a slower wave meant vortices were carried along with the wave where a faster wave caused them to lag behind and get caught in the material. This behavior makes sense, as there are several characteristic timescales which give the order parameter and other physical quantities some response time to changes such as temperature changes. When the temperature wave moves fast enough, the temperature is changing faster than the vortices have time to respond to, and therefore they are unable to keep up with the wave. We explore this kind of phenomenon more in Section 3.8.

3.4 Vortices Encountering Pinning Sites

Next, we wanted to see what happens when vortices are pushed towards pinning sites. The way we simulate a pinning site is by making a small island with different material parameters, like a smaller version of the islands pictured in Figure 2.1. To make the small island a pinning site, we give it the same H_c, λ, and γ as the rest of the material and a smaller T_c to ensure it has a harder time superconducting and therefore can trap or 'pin' magnetic field within it. In principle, we could choose to give the pinning site the parameters of a known material but as we are trying to get more of a qualitative sense of how superconductors behave under

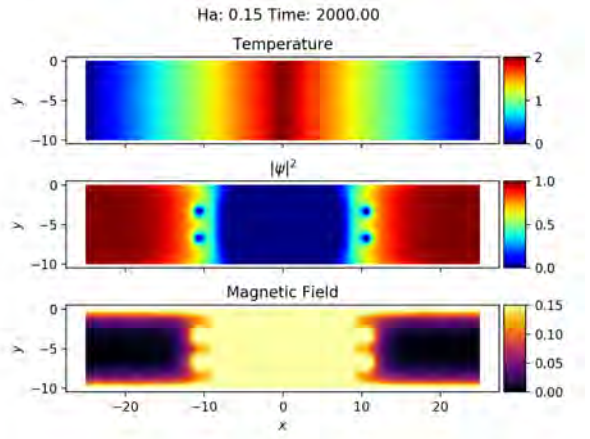

(a)

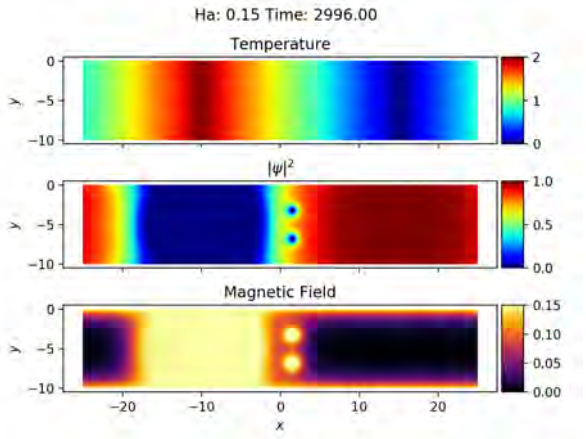

(b)

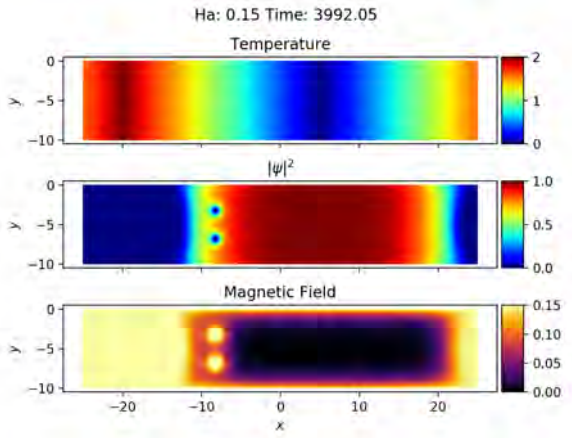

(c)

Figure 3.4: Vortices pushed by moving the temperature wave. In this case, the velocity of the wave is 0.0004. In (a) the vortices on the right start at $x = 10$, are pushed to about $x = 0$ in (b), and finally reach about $x = -10$ in (c). The vortices that were on the left at the start are absorbed into the normal region. This simulation was done at $H_a = 0.15$ to prevent new vortices from forming as the wave moves, which would push the existing vortices into the superconducting region. Since the simulation is periodic, running for a longer time would mean the vortices would keep getting pushed indefinitely, simply wrapping around to the other side of the domain.

different conditions, it is sufficient and much simpler to only vary T_c. A pinning site is stronger the closer T_c gets to 0.

Figure 3.6 shows a simulation where a pinning site with radius 0.25 and $T_c = 0.25$ is at (0, -7.5). When a vortex directly encounters the pinning site, it merges into it and becomes pinned to that site while the other vortex is pushed out of the superconducting region. In Figure 3.7, we run this simulation again except this time the pinning site has a T_c of 1.

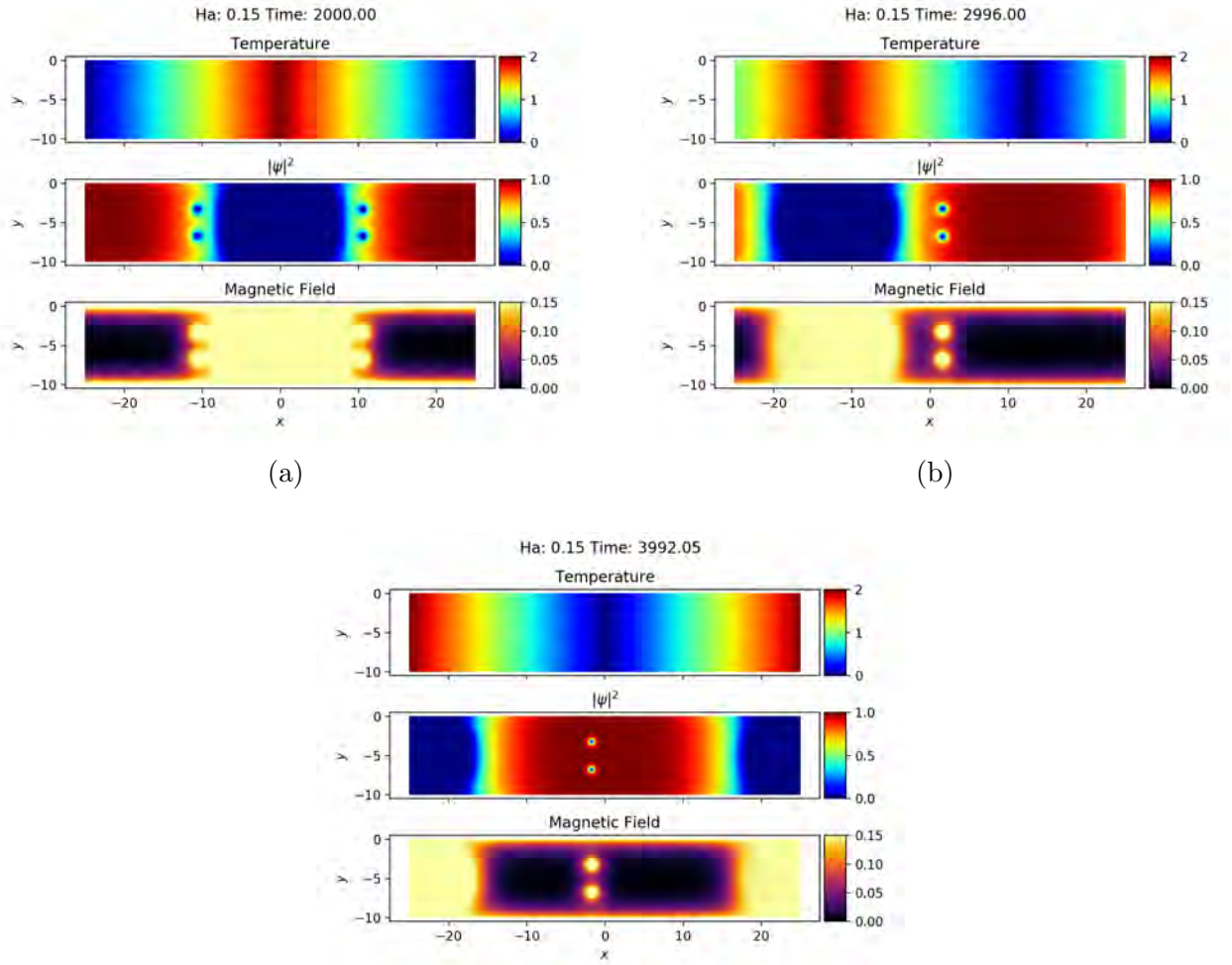

(a) (b)

(c)

Figure 3.5: Vortices pushed too fast by a moving temperature wave. The speed of the wave in this simulation is 0.0005. In (a), the vortices on the right start at $x = 10$, are pushed to about $x = 2$ in (b), but then lag behind, get stuck in the superconducting region, and only reach about $x = -2$ in (c). Notice how the vortices get smaller in terms of their size on the $|\psi|^2$ plot as they get stuck in the superconducting region, but the magnetic flux remains the same if you look at the magnetic field plot, because the magnetic flux of a vortex is quantized [9].

Initially the vortex again merges into the pinning site, however, this time the pinning site is not strong enough to keep the vortex pinned in the superconducting region, so as the wave proceeds, the vortex is pulled off the site and pushed along with the wave.

We then checked what would happen if the pinning site did not lie directly in the path of either vortex. In Figure 3.8, we placed a pinning site with radius 0.25, $T_c = 0.25$ at (0, -5), so that it would be directly between both vortices. This time, neither vortex was pulled

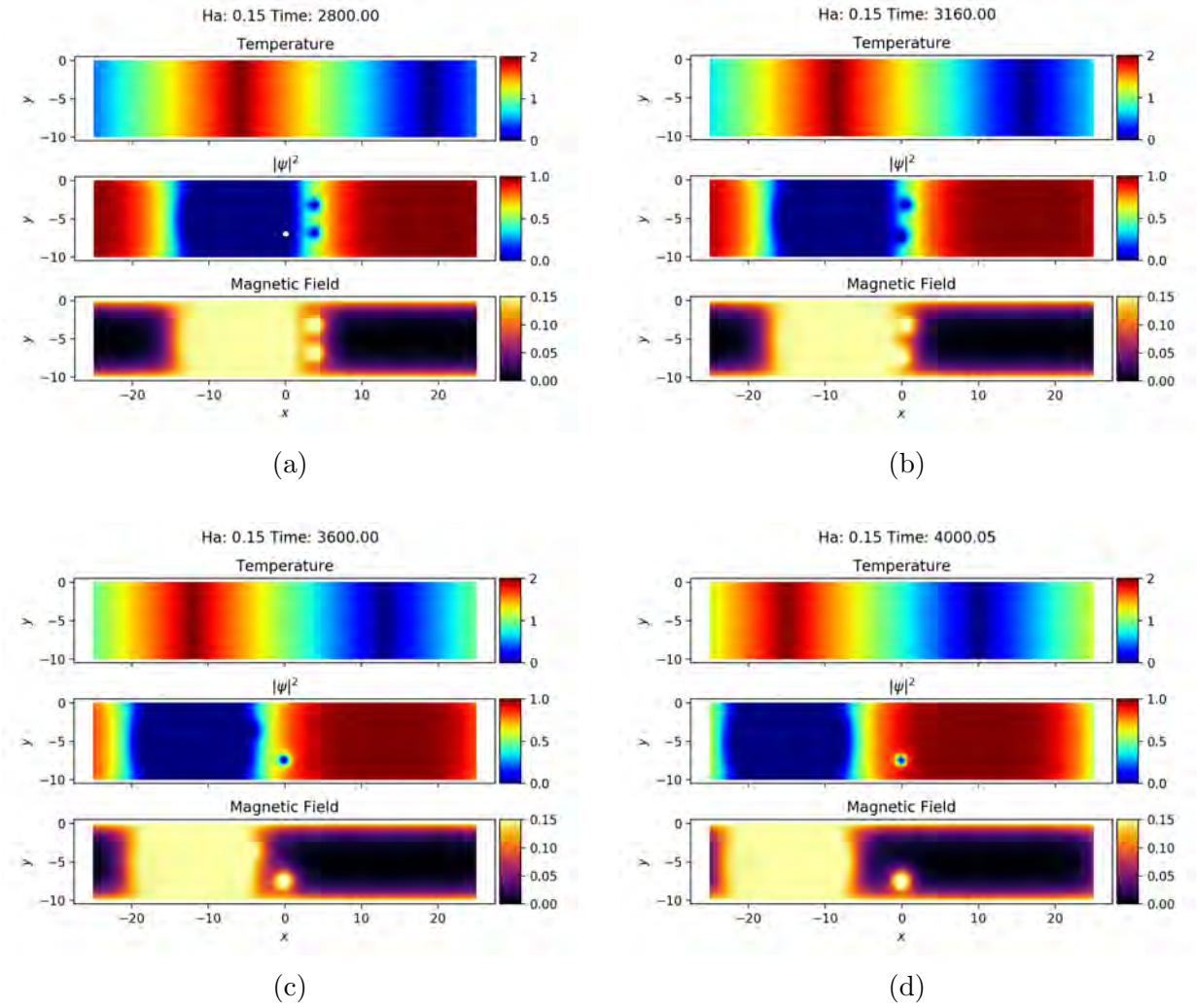

Figure 3.6: A vortex hitting a strong pinning site directly. (a) depicts the vortices being pushed towards $x = 0$, a circular pinning site of radius 0.25, $T_c = 0.25$, marked by a white dot is at (0, -7.5). In (b), the bottom vortex is pulled into the pinning site. In (c) and (d) the bottom vortex remains trapped in the pinning site as the other vortex is pushed out of the superconducting region.

into the pinning site and it passed between the two of them. It appears that the reason this happened is because, in addition to the aforementioned 'forces' vortices can experience, vortices repel one another. Due to this repelling, neither vortex was able to enter the pinning site and both vortices were successfully pushed out.

Finally, in Figure 3.9, we put another pinning site of radius 0.25, $T_c = 0.25$ at (0, -1). This was to see what happens if a pinning site does not directly encounter a vortex and also doesn't pass between two vortices. Here the vortex was pulled towards the pinning site,

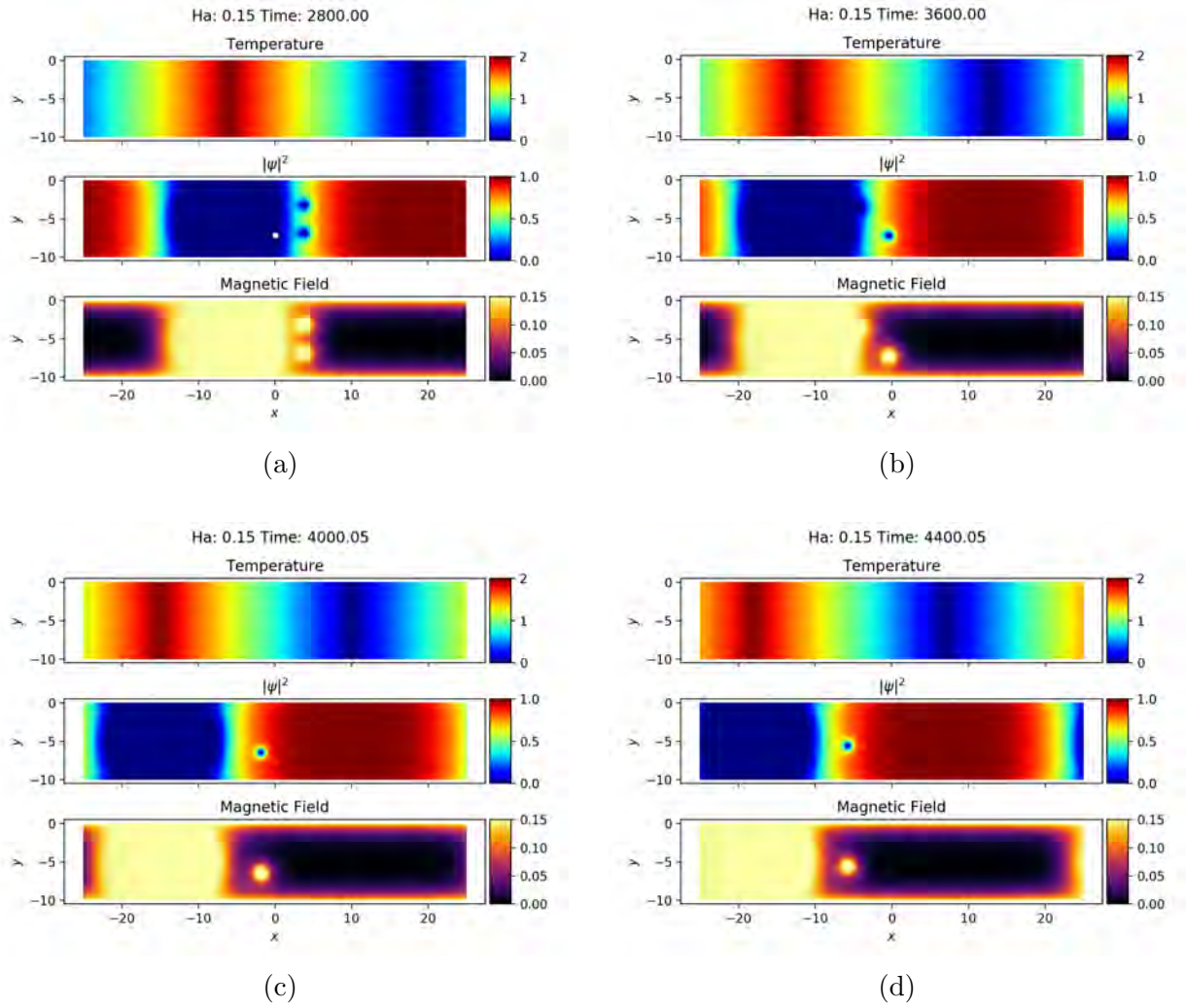

(a) (b)

(c) (d)

Figure 3.7: A vortex hitting a weak pinning site directly. (a) depicts the vortices being pushed towards $x = 0$, a circular pinning site of radius 0.25, $T_c = 1.0$, marked by a white dot is at (0, -7.5). In (b), the bottom vortex is pulled into the pinning site. In (c) and (d) the vortex fails to be trapped by the site and is swept away with the wave.

however since the pinning site was not close enough for the vortex to fall into it, it just pulled the vortex out of line with the lower vortex. The upper vortex still got pushed out with the wave. This resultant misalignment is significant because it is possible, that there could be another pinning site which would have passed through the vortices like the one in Figure 3.8, but since an earlier pinning site like the one in Figure 3.9 misaligned the two vortices, one of them could get stuck in the pinning site that otherwise might have passed through them.

These simulations have made it clear that the question of what happens when existing vortices encounter pinning sites is quite complex. If there are many more vortices, many

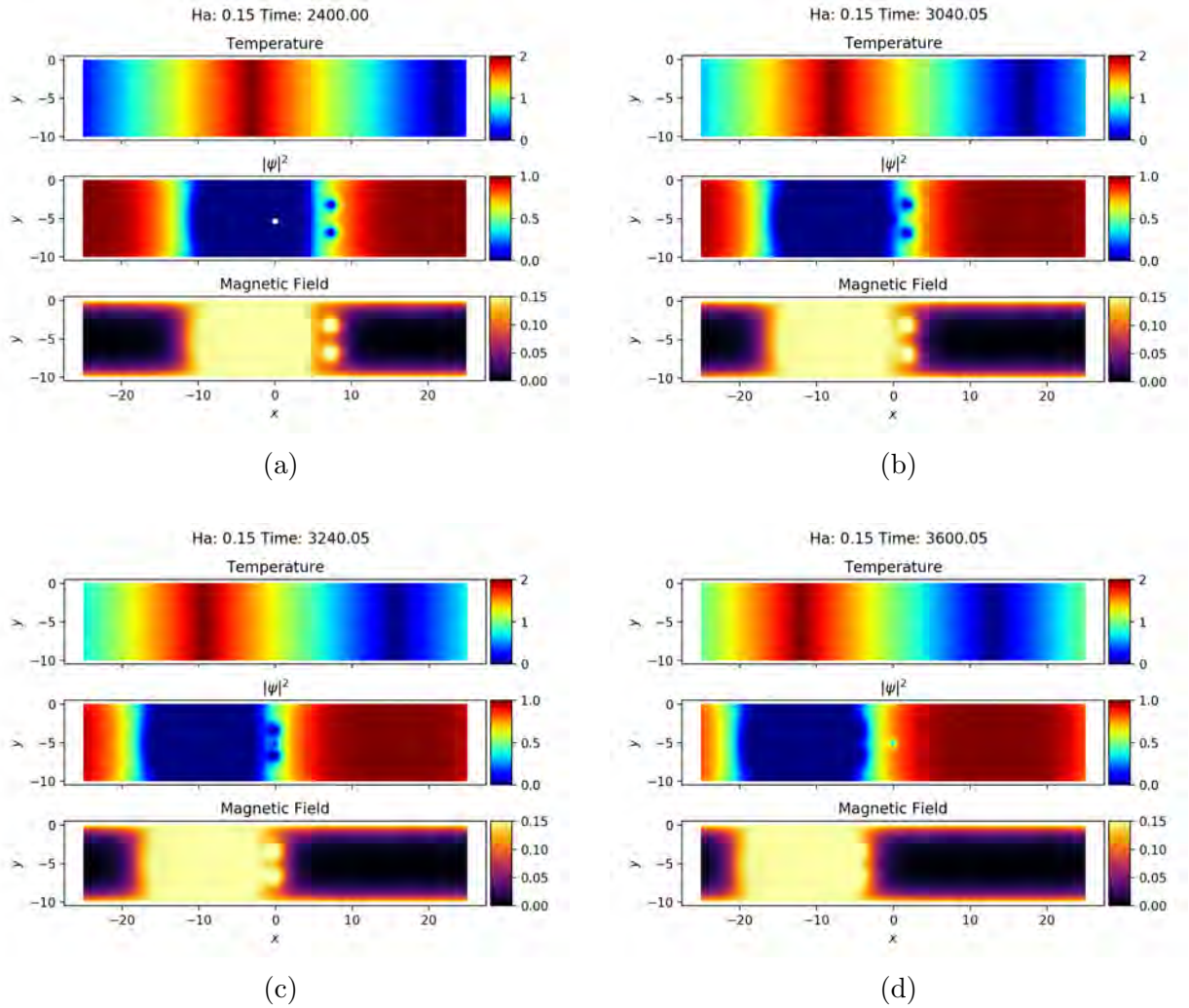

Figure 3.8: A pinning site between the path of 2 vortices. (a) depicts the vortices being pushed towards $x = 0$, a circular pinning site of radius 0.25, $T_c = 0.25$, marked by a white dot is at (0, -5). In (b), the wave first encounters the pinning site. In (c) and (d) the vortices repel each other so neither is able to be pulled into the pinning site and they pass through it. Notice how while $|\psi|^2$ is lower in (d) where the pinning site is, there is no magnetic field trapped there.

more pinning sites, or both, there quickly becomes a multitude of possible outcomes, as whether or not the vortices are pinned can depend on very small differences in the positions of vortices and pinning sites.

3.5 Vortices Encountering Grain Boundaries

Point-like defects such as pinning sites are not the only kind of defects in superconductors, there are also line defects realized by grain boundaries. These grain boundaries cause a

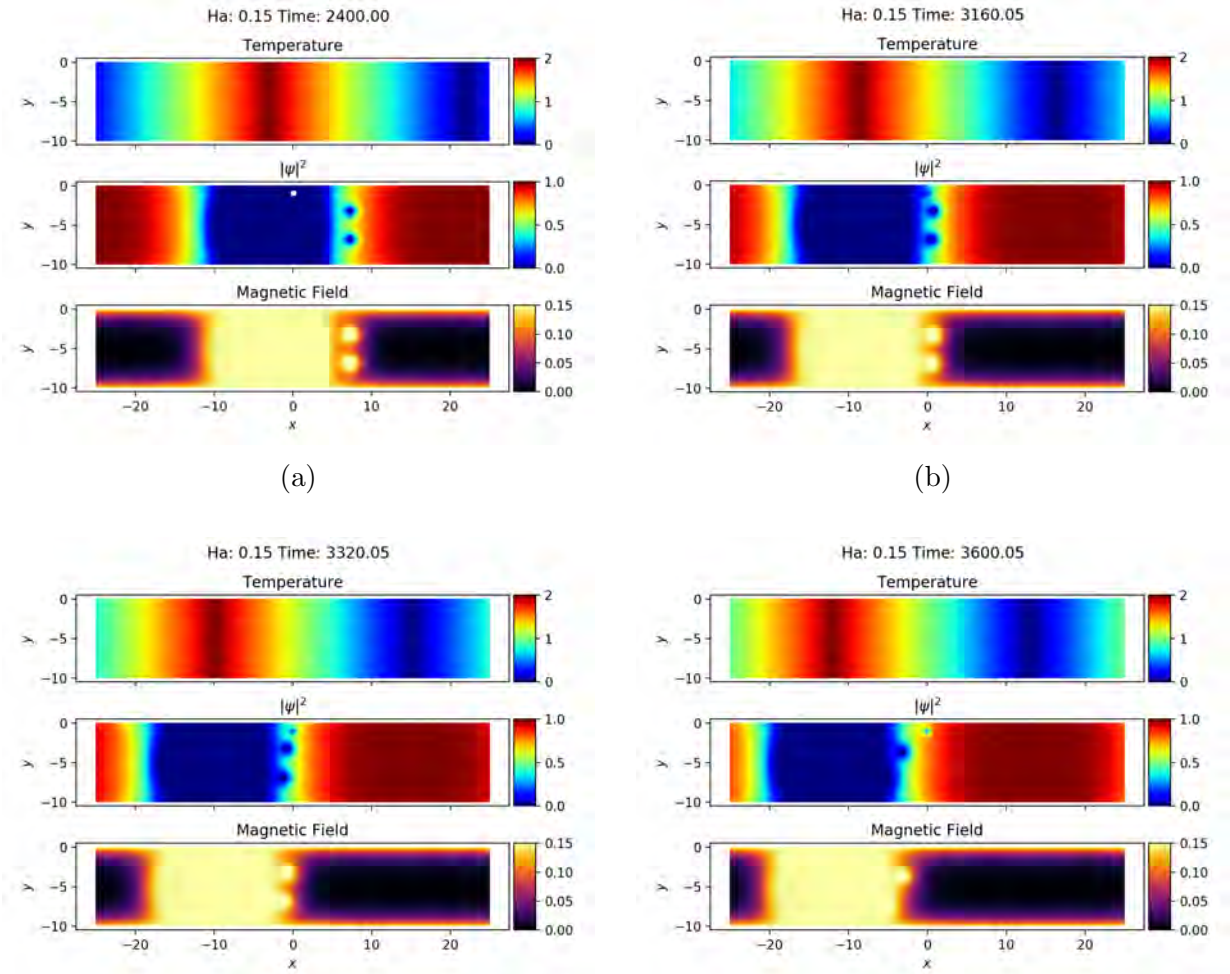

Figure 3.9: A vortex missing hitting a pinning site directly. (a) depicts the vortices being pushed towards $x = 0$, a circular pinning site of radius 0.25, $T_c = 0.25$, marked by a white dot is at (0, -1). In (b), the wave first encounters the pinning site and the upper vortex is slitghly pulled towards it. In (c) and (d) the upper vortex is attracted towards the pinning site, but not strongly enough to overwhelm the wave's push so the vortex is pushed out.

change in the effective material parameters of a superconductor due to inhomogeneities between different grains of a superconducting material [20]. Experimental studies [13] have determined that the grain structure of SRF cavities has a large impact on the amount of flux expulsion that occurs. Grain boundary simulations can allow us to explore the partial cause of this result.

We first started by looking at horizontal grain boundaries, Figure 3.10 such a simulation. Here we have a horizontal grain which we implement by creating an island in the shape of

an ellipse with a semi-major axis of 5 and a semi-minor axis of 0.3 centered at (0, -7.5). This particular grain has a T_c of 1, with all the other material parameters unchanged, as has been standard throughout this work. We see that, just like for a similar pinning site at the same y value such as in Figure 3.7, the vortex is pulled into the grain boundary; however, in this situation the vortex has some freedom to move along the grain boundary, so unlike the pinning site, the vortex remains in the grain boundary after the wave passes. In this case the grain boundary was able to trap magnetic flux where a pinning site was not.

This effect is also seen if we move the grain boundary to have it's center at (0, -5.0), shown in Figure 3.11. Here the grain boundary is between the two vortices, yet both of them get pulled into it and spread apart. This is in stark contrast to Figure 3.8, where the pinning site only has space for a single vortex and so they both repel and the pinning site passes between the two. Yet again, the grain boundaries seem to have a much easier time trapping vortices.

We also looked at a vertical grain boundary, to see if the orientation of the grain had an effect, shown in Figure 3.12. In this case we used a boundary which entirely split our domain across $x = 0$ and had a width of 0.6 and a T_c of 1. As the vortices are pushed towards the vertical grain boundary, they fall into the grain and are stuck there. It should be noted that this vertical grain boundary is somewhat different from the horizontal grain boundary, as not only is it perpendicular to the movement of the vortices, but it also extends to the top and bottom of the domain, which means the magnetic field can enter it easily, since this is where the magnetic field is applied.

All the grain boundaries in this section had $T_c = 1$. We also ran all these simulations for $T_c = 0.25$; however, we have not to included these plots as they show qualitatively similar results, with the vortices getting pinned anywhere they came in close contact with a grain boundary. These simulations have shown that grain boundaries seem to have a much larger potential for trapping vortices than pinning sites.

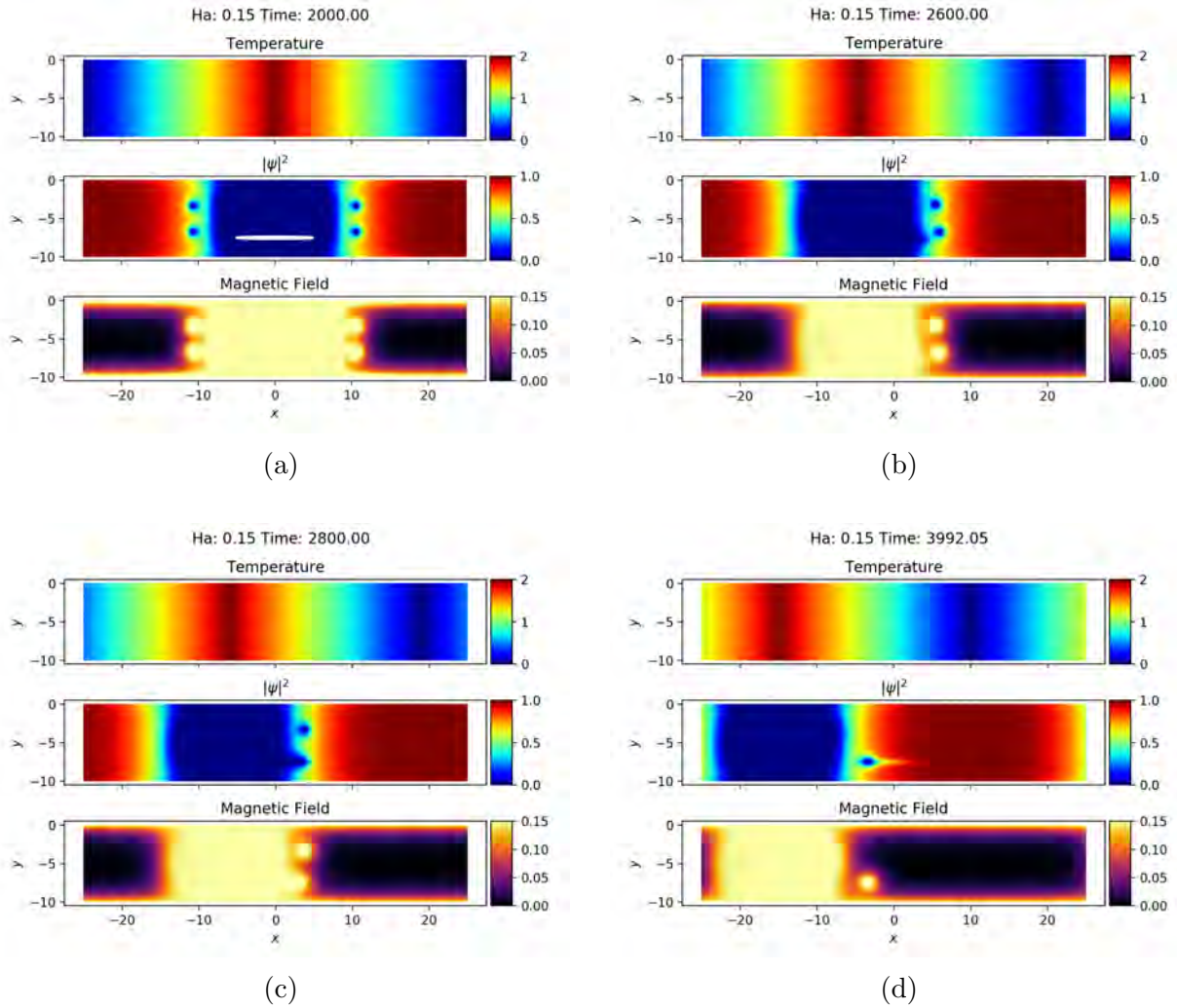

Figure 3.10: A vortex pushed into a horizontal grain boundary. (a) is the starting position of the vortices. There is a horizontal grain boundary in the shape of an ellipse with a semi-major axis of 5 and a semi-minor axis of 0.3 centered at (0, -7.5) with $T_c = 1$. This grain is marked by a white ellipse of the same shape. In (b), the lower vortex first encounters the grain. The vortex is then pulled into the grain, shown in (c). In (d), the lower vortex has been pushed along the grain by the temperature wave but remains pinned while the other vortex is pushed out.

3.6 Vortex Nucleation in Pinning Sites

Up to this point, we've been looking at what happens when existing vortices encounter material defects such as pinning sites or grain boundaries. Next we look at the ability of defects to nucleate new vortices. To answer this, we first lower H_a to 0.1, which forces any vortices out of the superconducting regions. Then we put a pinning site at (0, -5) and move the wave at a speed of 0.0003. There are two important parameters we decided are relevant

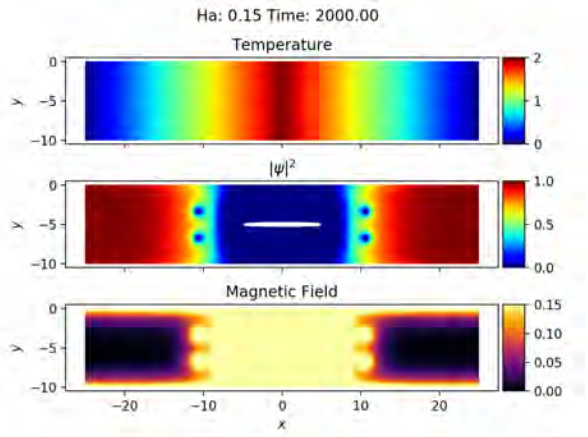

(a)

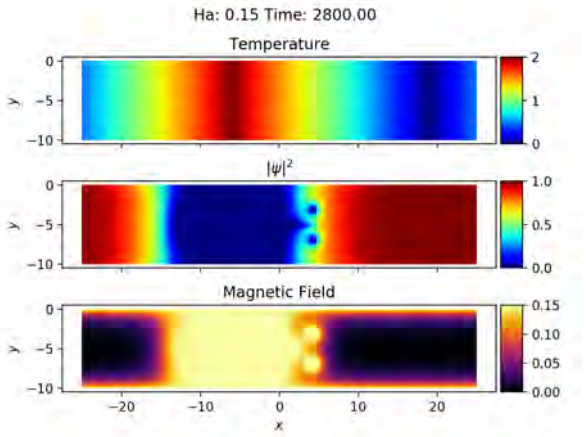

(b)

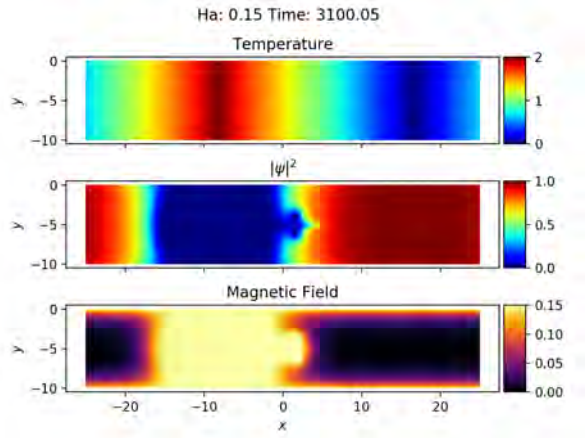

(c)

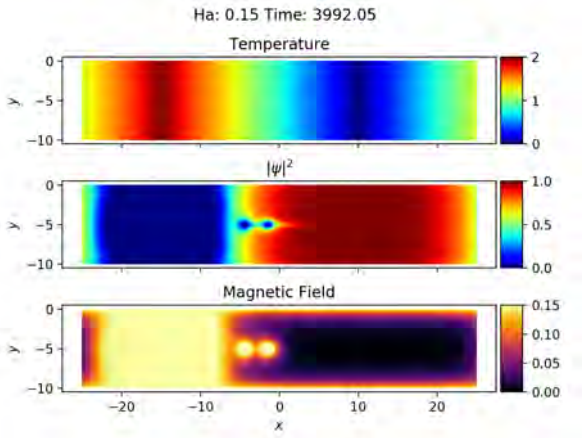

(d)

Figure 3.11: A pair of vortices pushed into a central horizontal grain boundary. (a) is the starting position of the vortices. There is a horizontal grain boundary in the shape of an ellipse with a semi-major axis of 5 and a semi-minor axis of 0.3 centered at (0, -5) with $T_c = 1$. This grain is marked by a white ellipse of the same shape. In (b), the vortices have encountered the grain and it appears that it could go between them, such as the pinning site in Figure 3.8. By (c), the vortices seem to be pulled into the grain instead. At (d), both vortices have become pinned to the grain boundary.

for determining whether a pinning site will nucleate a new vortex: pinning site size and pinning strength. We ran simulations for several different pinning site radii and pinning strengths. Figure 3.13 shows a simulation for a pinning site with radius 0.4 and $T_c = 1$. In this simulation the pinning site does slightly impact the wave, but it ultimately does not manage to pin a vortex.

Figure 3.14 depicts a simulation similar to the previous one, except the pinning is twice

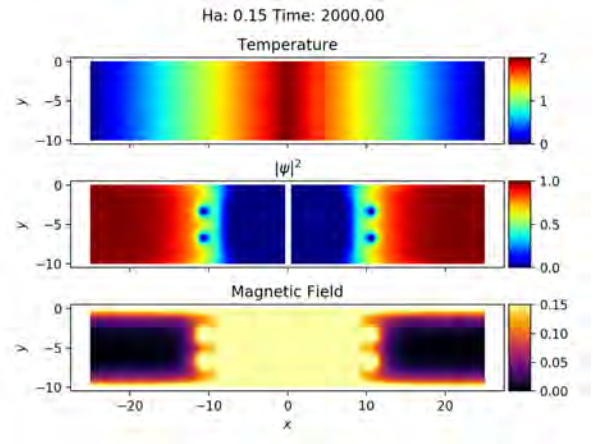

(a)

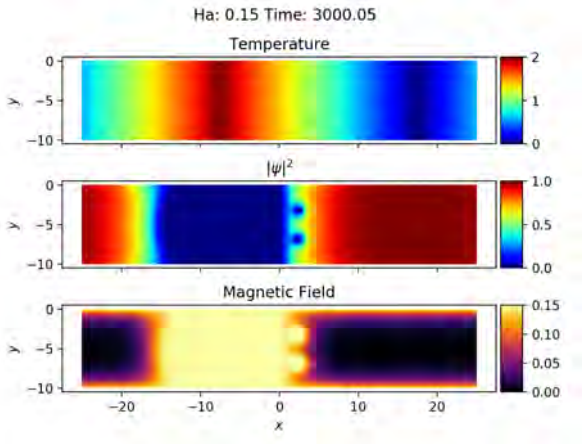

(b)

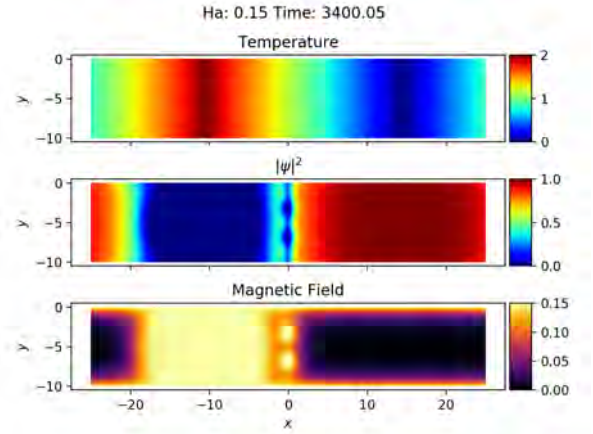

(c)

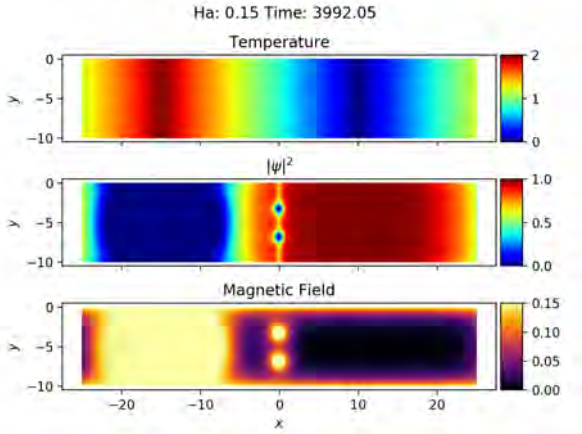

(d)

Figure 3.12: A pair of vortices being pushed into a vertical grain boundary. (a) is the starting position of the vortices. There is a vertical grain boundary of width 0.6 centered at $x = 0$ with $T_c = 0.25$. This is marked by a white rectangle of the same shape. In (b) the wave has reached the grain boundary, and the vortices are pulled toward it. In (c) the vortices are pinned to the grain boundary, and they remain pinned as the wave moves on in (d).

as strong with a T_c of 0.5. In this simulation, the pinning site is able to successfully nucleate a vortex. We ran 20 simulations, all of which look more or less like Figure 3.13 or Figure 3.14, so rather than including all of them, Table 3.1 shows the results of these simulations in terms of whether or not a vortex was nucleated. Notably, it seems the size of the pinning site is much more impactful than the strength of the pinning site; a site with radius 0.3 failed to pin a vortex for any pinning strength, whereas a pinning site of radius 0.4 or 0.5 pinned a vortex for all $T_c \leq 0.5$, and a radius of 0.6 pinned some magnetic field every time.

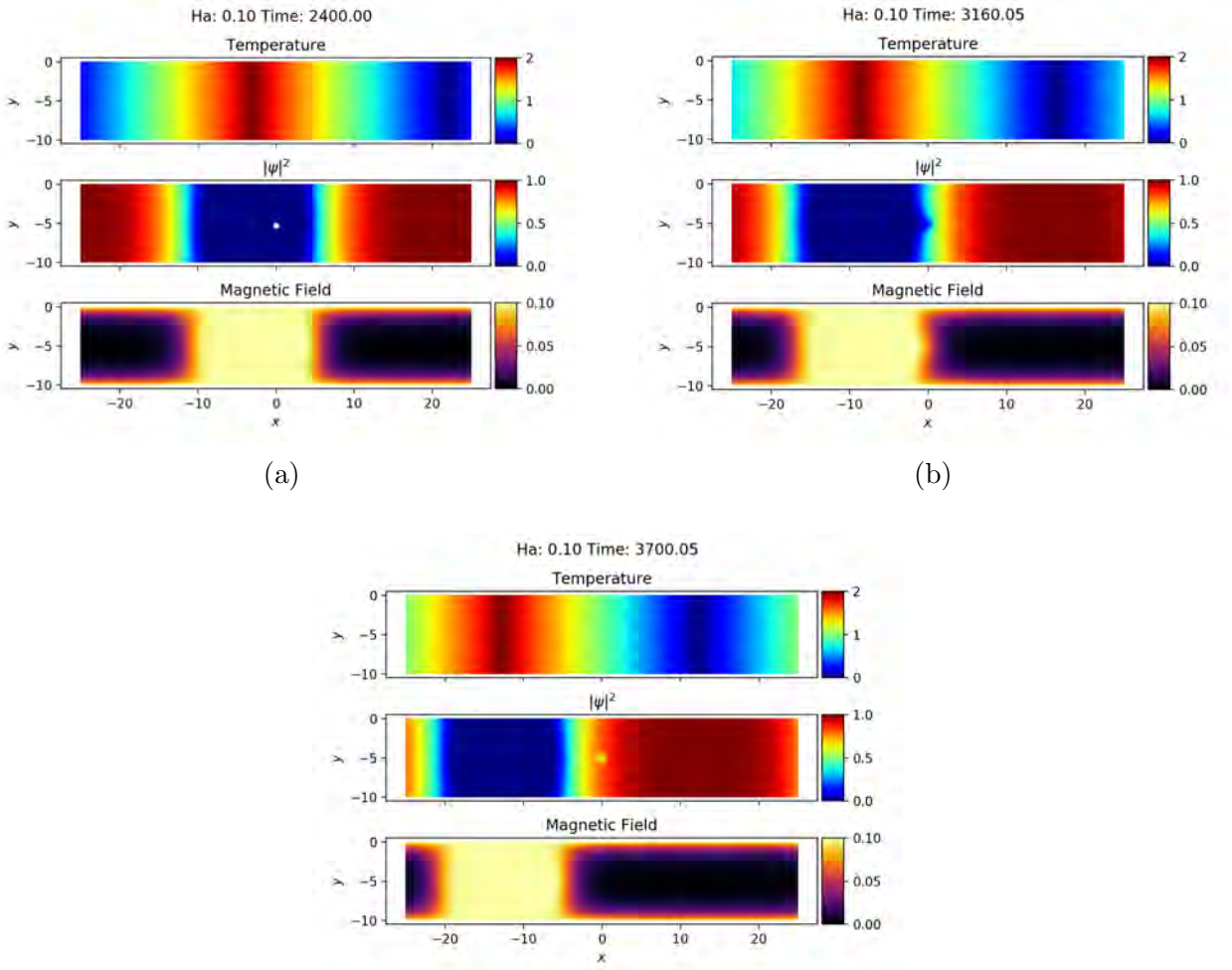

(a) (b)

(c)

Figure 3.13: A weak pinning site fails to nucleate a vortex. (a) depicts a pinning site of radius 0.4, $T_c = 1$ marked by a white dot. In (b), the temperature wave (moving at $v = 0.0003$) moves to where the superconducting transition region is above the pinning site and some magnetic field enters that region. Ultimately in (c), the site is not strong enough to pin a vortex and no magnetic field is trapped despite a lower $|\psi|^2$ where the pinning site is.

r \ T_c	1	0.5	0.25	0.1	0.01
0.3	*No*	*No*	*No*	*No*	*No*
0.4	*No*	*Yes*	*Yes*	*Yes*	*Yes*
0.5	*No*	*Yes*	*Yes*	*Yes*	*Yes*
0.6	*Yes*	*Yes*	*Yes*	*Yes*	*Yes*

Table 3.1: Magnetic flux pinning ability with respect to pinning site radius and strength. The left column shows the values of the radius r of a circular pinning site centered at (0, -5). The top row is the T_c of the pinning site, smaller values means stronger pinning. A No indicates that a vortex was not pinned, a Yes indicates that a vortex was pinned.

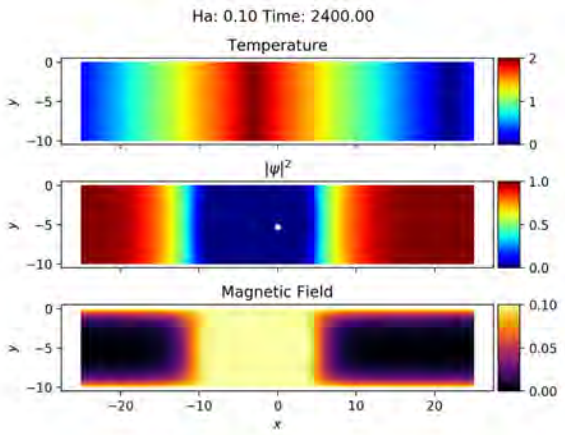

(a)

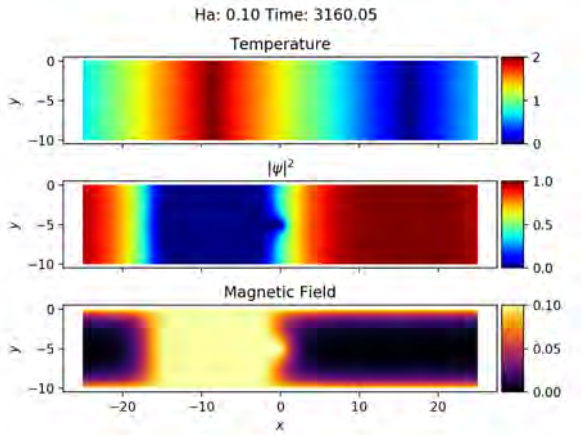

(b)

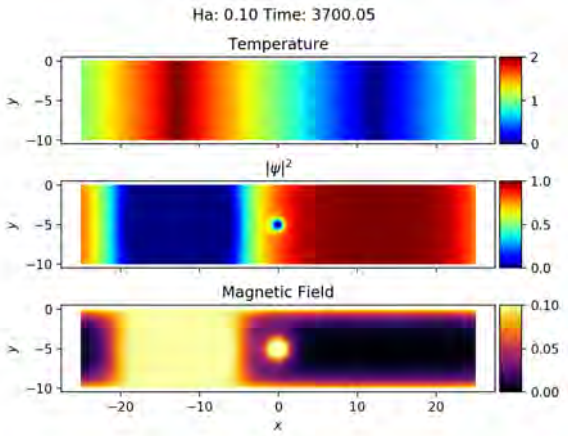

(c)

Figure 3.14: A strong pinning site nucleates a vortex. (a) depicts a temperature wave in the process of moving towards a pinning site of radius 0.4, $T_c = 0.5$ marked by a white dot. (b) shows the wave encountering the pinning site, and the magnetic field entering that region more substantially than in Figure 3.13. Ultimately in (c), the site is strong enough to pin a vortex.

In our simulations, κ_0 is inversely proportional to the size of a vortex, and since we use $\kappa_0 = 4$, this means the radius of a vortex will be approximately $\frac{1}{4}$. Thus Table 3.1 seems to indicate that a pinning site radius of 0.3 is too small for a vortex to be able to fully form inside it. Pinning sites of this size can only trap existing vortices, this behavior is seen in the simulations discussed in Section 3.4. Conversely, if a pinning site is large enough to fit a vortex inside it (which seems to be the case for an r of at least 0.4), a vortex will nucleate unless the pinning is very weak. For $r = 0.6$, a vortex was pinned regardless of the pinning

strength.

3.7 Vortex Nucleation in Grain Boundaries

We also looked at the ability of grain boundaries to nucleate new vortices. In Figure 3.15, our temperature wave passes through a horizontal grain boundary with $T_c = 0.25$. It ends up nucleating two vortices with ease, suggesting that it is likely quite easy for grain boundaries to form vortices when cooling fronts go by them in a perpendicular direction. This is further confirmed when looking at Figure 3.16. In these plots, the horizontal grain boundary has a T_c of 1, the same strength as the pinning site in Figure 3.13, where a vortex was not successfully pinned. With a horizontal grain boundary of the same strength, the extra time and resistance the order parameter faces as the temperature wave passes over a weak but much longer defect allows a vortex to nucleate and sit in the weak grain boundary.

Similarly, for a vertical grain boundary with $T_c = 0.25$, as shown in Figure 3.17, two vortices end up in the grain after the cooling front passes, though this could partially be due to the fact that the applied magnetic field is able to directly enter the grain boundary at the top and bottom of the domain. The same thing happens for a vertical grain boundary of $T_c = 1$, except only one vortex ends up in the grain instead of two,

Overall, grain boundaries seem like prime candidates for trapping vortices and decreasing SRF cavity performance. While pinning sites only really have the ability to pin vortices if they are larger defects, grain boundaries seem to easily trap vortices, even if they are a rather weak defect to begin with. Larger defects are uncommon in well made SRF cavities, whereas even the most well made cavities can contain many grain boundaries. Experimental data from [13] seems to agree with this result, as SRF cavities exhibited stronger flux expulsion when they were given a heat treatment which increases grain size, therefore decreasing the number of grain boundaries.

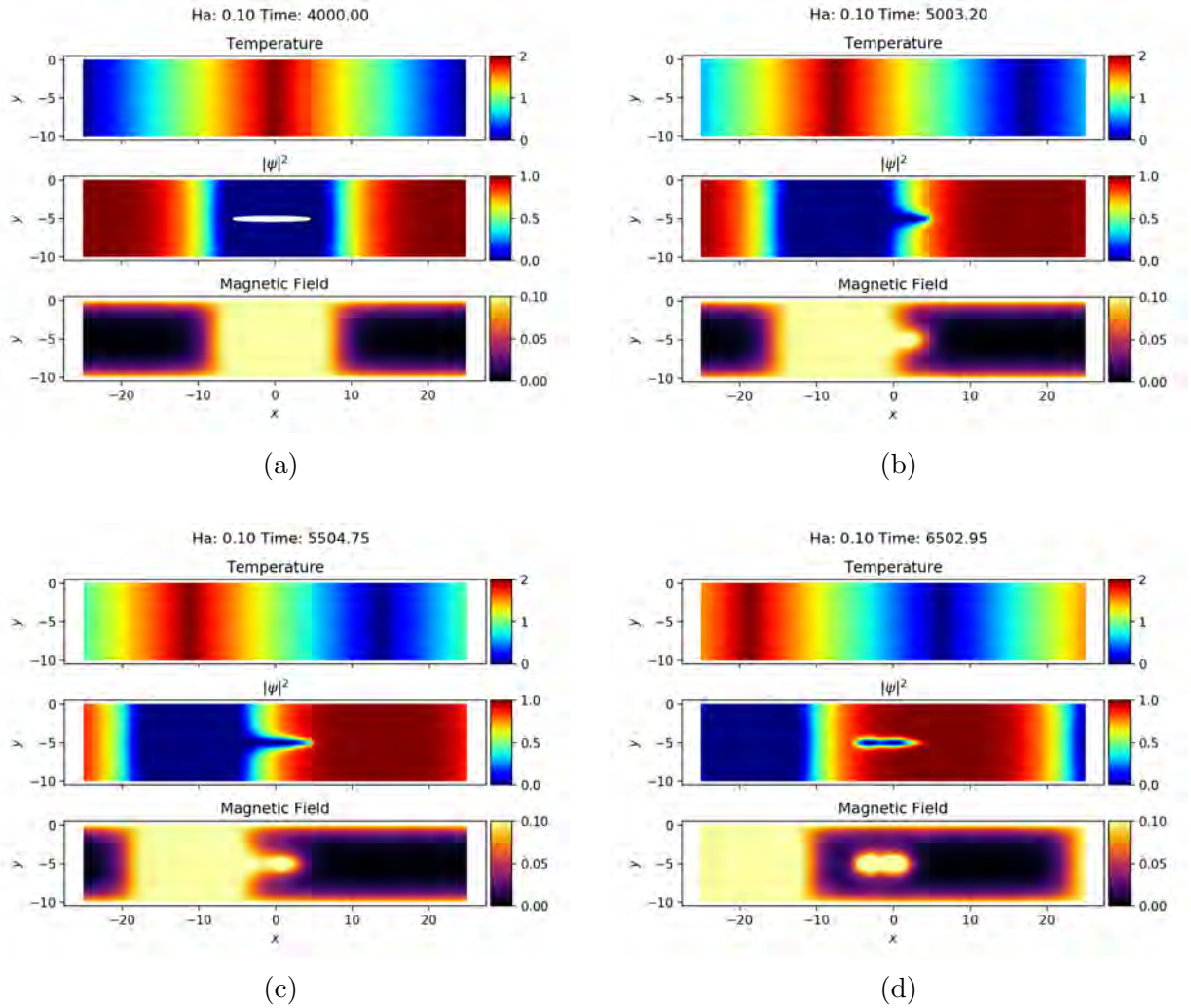

(a) (b)

(c) (d)

Figure 3.15: A temperature passing a horizontal grain boundary with $T_c = 0.25$. (a) is the starting position of the wave. There is a horizontal grain boundary in the shape of an ellipse with a semi-major axis of 5 and a semi-minor axis of 0.3 centered at (0, -5) with $T_c = 0.25$. This grain is marked by a white ellipse of the same shape. In (b), the wave passes through the grain boundary and magnetic field is pulled into this part of the domain. By (c), at least one vortex seems to have formed fully in the grain, according the the magnetic field plot. At (d), the temperature wave has passed the grain and there are two vortices left behind in the grain. Note that since the grain is very anisotropic, the vortices are ellipses rather than the usual circles.

3.8 Effect of Varying u_0 on Vortex Speed

The time dynamics of materials are very important in the simulations we have discussed thus far, so it makes sense to explore what happens when we vary u_0 and therefore change the time dynamics. As a reminder, u_0 is a ratio of two timescales which control the response times of

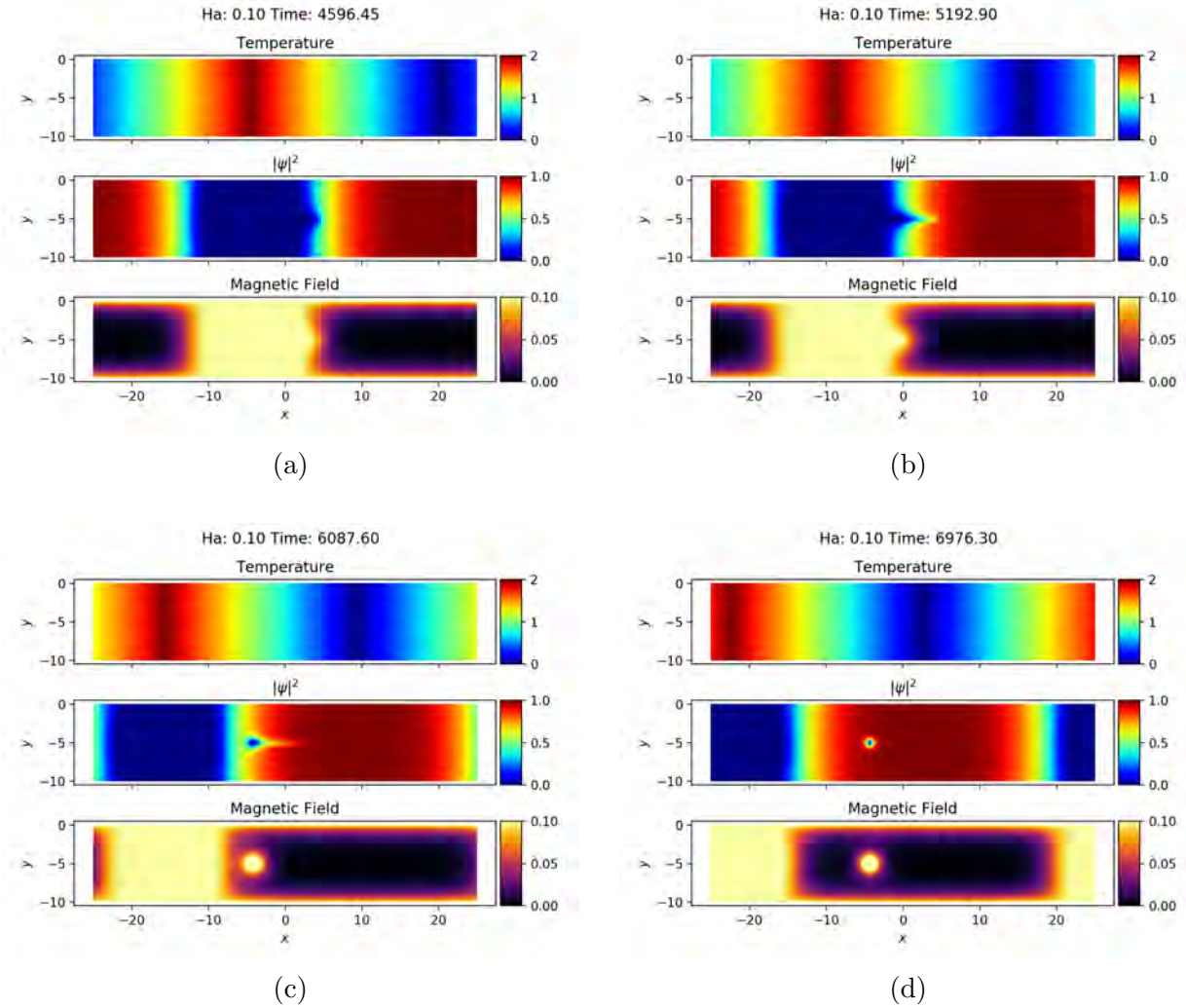

Figure 3.16: A temperature wave passing a weak horizontal grain boundary. (a) is the starting position of the wave. There is a horizontal grain boundary in the shape of an ellipse with a semi-major axis of 5 and a semi-minor axis of 0.3 centered at (0, -5) with $T_c = 1$. This grain is marked by a white ellipse of the same shape. In (b), the wave passes through the grain boundary and a small magnetic field is pulled into this part of the domain. By (c), one vortex has been pulled off and the wave has moved on. At (d), the single vortex has settled into place on the left side of the grain. Note that in contrast to Figure 3.15, this vortex is circular since the grain is not strong enough to alter the vortex shape.

ψ and $\mathbf{A}$. We initially looked at the speed of a vortex under a linear temperature gradient with the same slope as our triangle waves. Doing so, we generated the plots in Figure 3.18, where v_{vort} is the speed at which the vortex is pushed by the temperature gradient. We varied u_0 between 0.5 and 10 and seem to be observing a logarithmic relationship between u_0 and v_{vort}, this is confirmed by the exponential-like relationship between $\ln(u_0)$ and v_{vort}, which suggests that continuing to raise u_0 will continue to increase v_{vort}. It should be noted

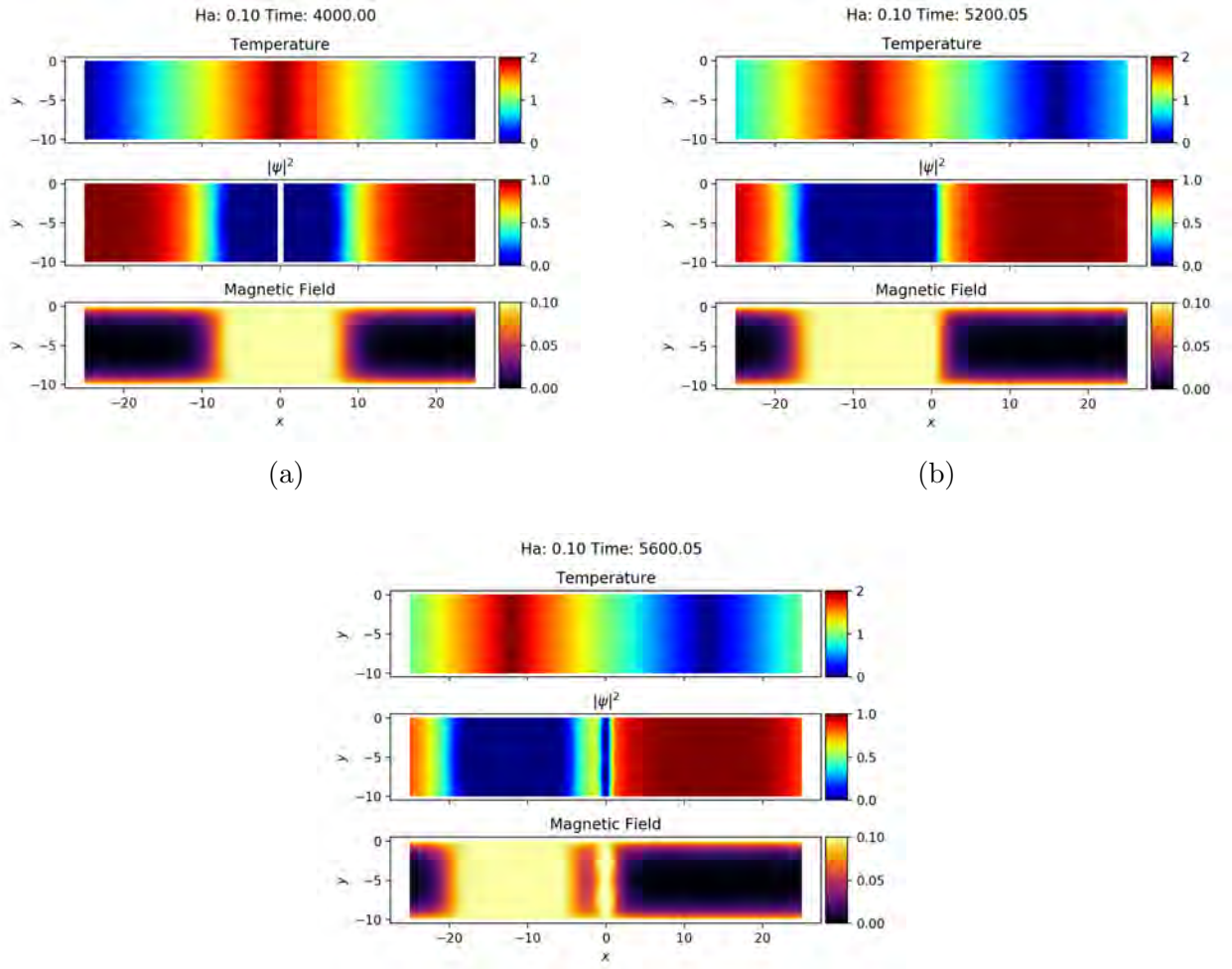

(a) (b)

(c)

Figure 3.17: A cooling wave passing a vertical grain boundary. (a) is the starting position of the wave. There is a vertical grain boundary of width 0.6 centered at $x = 0$ with $T_c = 0.25$. This grain is marked by a white rectangle of the same shape. In (b) the wave has reached the grain boundary and stops moving. After a little time passes, in (c) the material on the other side of the grain begins superconducting and the wave moves on. Note how there are two anisotropic vortices in the grain boundary, but the whole boundary is filled with magnetic field. This is because the magnetic field is applied at the top and bottom of the domain so it can easily enter into the grain here.

that while this is the case, higher values of u_0 require much smaller simulation time steps which can make the calculations considerably more computationally expensive. Additionally, the superconductors used in SRF cavities can have a u_0 of up to 5.79 [17]; other materials could theoretically have larger values, but there is not much value in investigating higher than $u_0 = 10$ unless it can be shown that there are different qualitative behaviors above that threshold.

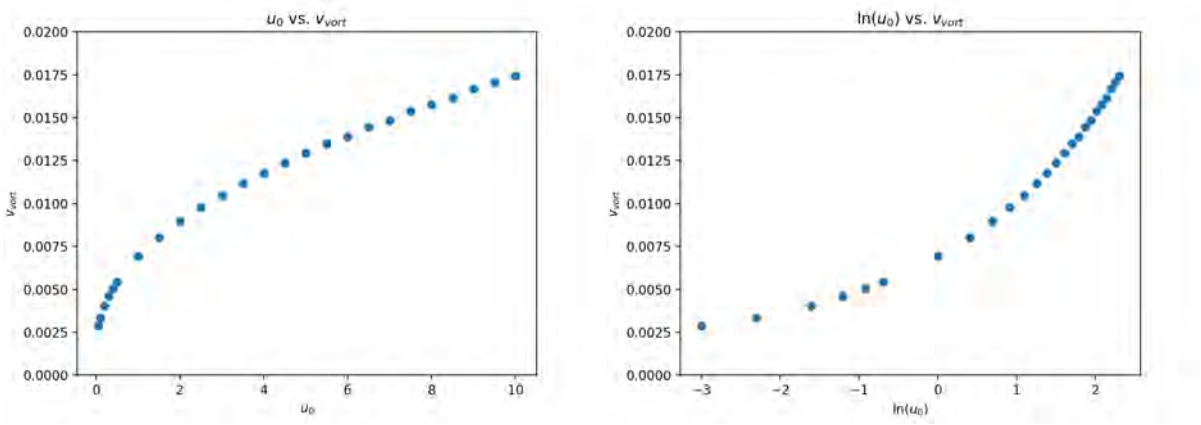

(a) (b)

Figure 3.18: Plot of u_0 and $\ln(u_0)$ versus v_{vort}. These plots were generated by putting a vortex under a constant temperature gradient and measuring the speed at which it is pushed. u_0 impacts the time dynamics of our simulations, as shown in (a). Increases in u_0 allows for a faster vortex speed within our simulations. (b) shows a log-linear plot of the same data, which appears exponential.

3.9 Varying u_0 and Temperature Wave Speed

In another set of simulations we considered temperature waves with no vortices or pinning sites moving at different speeds v_{wave}, once again using Equation 3.1.1 as our temperature function. At a high enough v_{wave}, the temperature wave moves faster than the superconducting region can easily keep up with and vortices end up getting 'peeled' off the normal region of the domain, getting stuck in the superconducting region. Figure 3.19 depicts this phenomenon. We initially used a u_0 of 1, but we then decided to run simulations for many different combinations of u_0 and v_{wave} to map out where this phenomenon happens. The results of these simulations are summarized in Figure 3.20.

Once again we see that a higher u_0 allows for faster dynamics. In this case it allows the superconducting region to respond faster to the change in temperature so that new vortices are not 'peeled' off the normal region. The threshold at which vortices start to nucleate seems to have a roughly linear relationship with respect to u_0. The equation this threshold follows is approximately $v_{threshold} = 0.00147u_0 + 0.00069$.

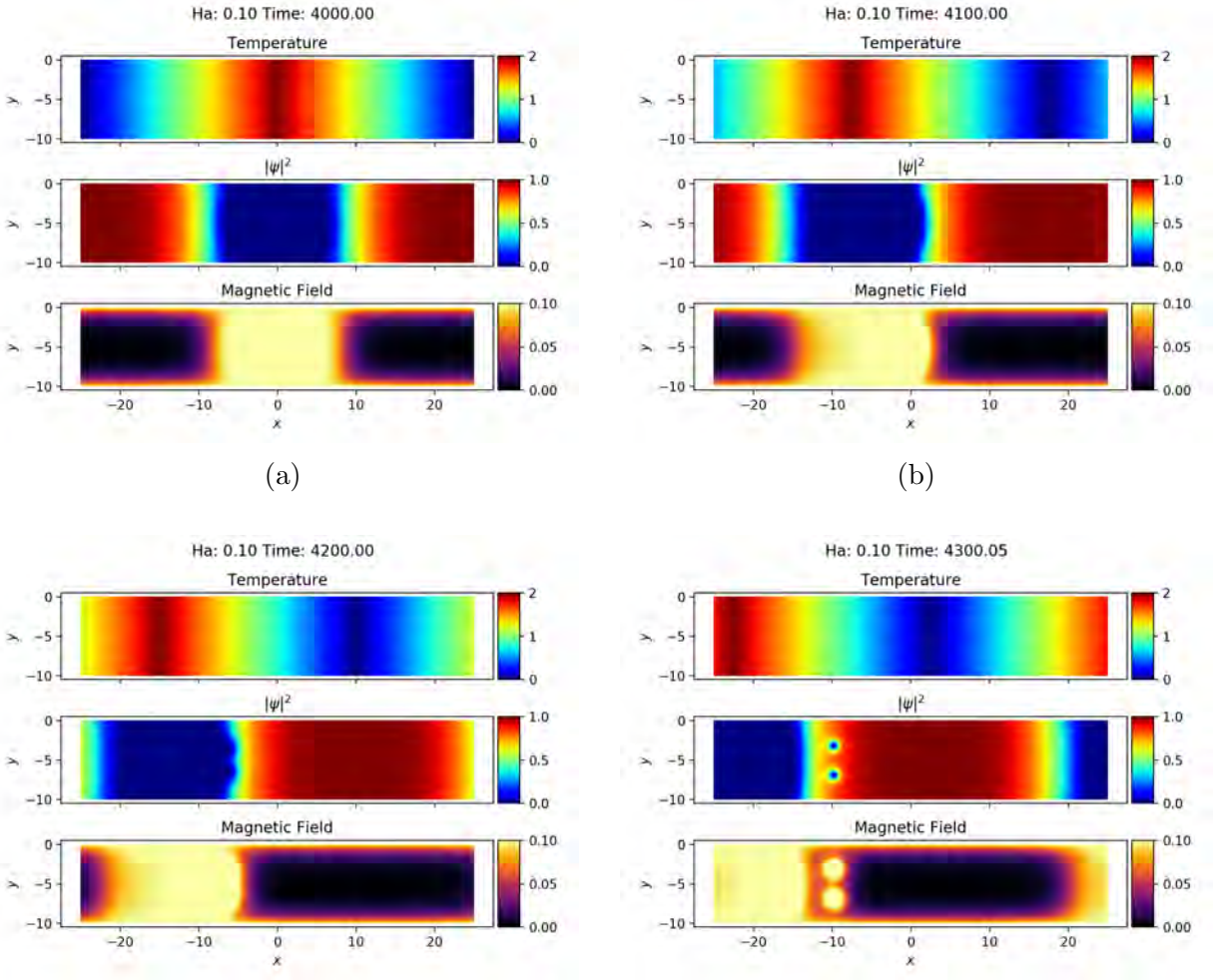

(a) (b)

(c) (d)

Figure 3.19: A set of vortices peeling off a fast temperature wave. Here $u_0 = 1$ and the wave is moving at $v_{wave} = 0.003$. The wave begins where it is pictured in (a). Shown in (b), a bulge begins to form in the normal region as the superconducting region is unable to keep up with the temperature changes. By (c) two smaller, vortex-sized circular bulges have formed. In (d) these bulges have become vortices which get stuck in the superconducting region since the wave is moving too fast, similar to what happens in Figure 3.5.

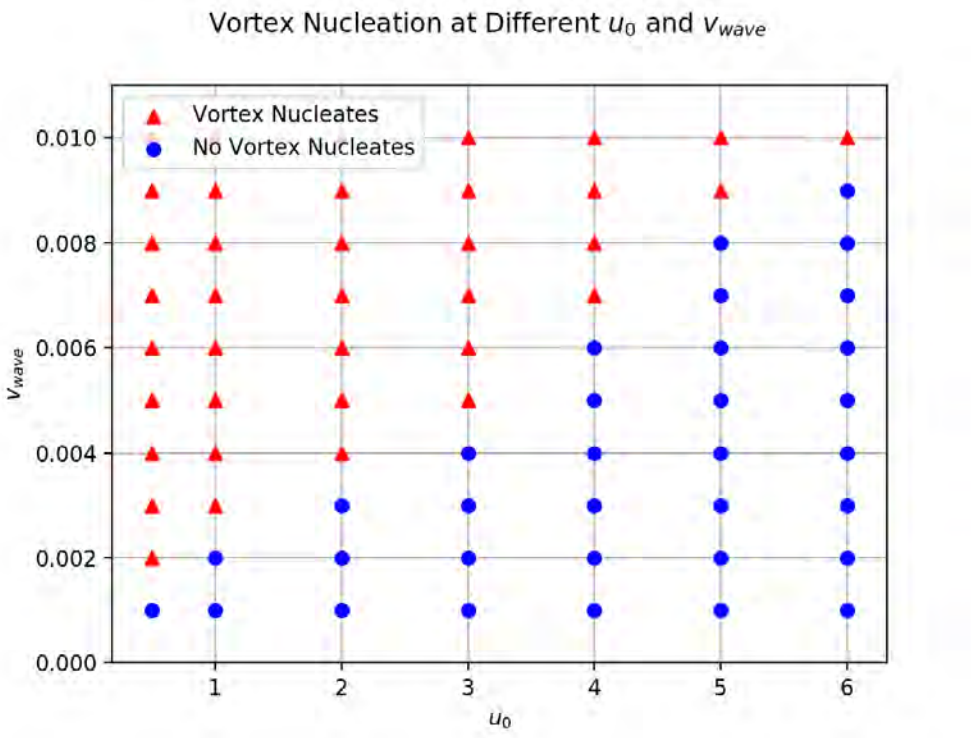

Figure 3.20: Vortex nucleation at different u_0 and v_{wave}. The red triangles represent simulations in which vortices were 'peeled' off the normal region. The blue circles are simulations in which this did not happen and the superconducting region moved through the domain uneventfully.

Chapter 4

Conclusions and Future Work

We showed many results and simulations in Chapter 3. The purpose of this chapter is to summarize the important takeaways from these simulations, discuss their potential implications for SRF cavity construction and operation, and suggest some future simulations and code adaptations.

4.1 Conclusions

Broadly speaking, there are 6 categories of simulations we ran: pushing vortices with temperature waves, pushing vortices into pinning sites with temperature waves, pushing vortices into grain boundaries with temperature waves, testing pinning site vortex nucleation ability, testing grain boundary vortex nucleation ability, and investigating the effects of varying u_0. From these simulations we found that vortices can be pushed by moving temperature gradients; however, moving them too fast means the vortices will lag behind and get stuck in the superconducting region, potentially allowing new vortices to enter the mixed state region. If these vortices encounter pinning sites, the end result gets even more complicated. Direct encounters with pinning sites can cause vortices to become pinned as long as the site is sufficiently strong. Pinning sites can also pass through two repelling vortices unaffected, or slightly pull on a single nearby vortex without actually pinning it. Overall, pinning sites are more often than not unable to trap existing vortices, assuming these pinning sites are not large. Grain boundaries, on the other hand, have a large affect on existing vortices, trapping a vortex in almost any situation where it gets near a grain boundary. Even the weakest

grain boundaries we simulated still ended up pinning magnetic flux. When looking at defects' ability to pin magnetic field without encountering existing vortices, pinning sites again have little to no effect unless the pinning sites are larger than a vortex, in which case they will almost always pin some magnetic field regardless of pinning strength. Grain boundaries again also have a large impact, consistently pinning magnetic field even for low strength grain boundaries. Finally, we found that increasing u_0 allows vortices to move faster, and allows us to move temperature waves faster without any vortices nucleating due to the wave moving too fast.

In terms of SRF cavity construction, our results seem to confirm existing hypotheses that keeping any material defects small and getting the average grain size to be as large as possible to reduce grain boundaries is the easiest way to improve the efficiency of magnetic flux expulsion from SRF cavities [13]. As for SRF cavity cooling and operation, our results are slightly less conclusive. While we have found that faster changes in the order parameter tend to result in extra vortices entering the superconducting regions, the time frames for even the slowest simulations here are on the scale of microseconds. As discussed in Section 1.2, macroscopic changes in cooling protocols (which take much longer than microseconds) are what seem to be having an effect on magnetic flux expulsion experimentally. Revisiting some of our simulations, when a wave is moving fast the mixed state region where the order parameter is transitioning from a normal metal to superconducting becomes slightly compressed, such as in Figure 3.19 (b), more than it is when a wave moves slowly, such as in Figure 3.17 (a). It could be the case that a slower injection of liquid helium means the width of this mixed region ends up being smaller than quickly blasting the cavity with helium and creating a more 'smeared out' mixed region. The simulations in which the mixed region is compressed are the simulations where more vortices tend to get stuck in the superconducting regions, so perhaps this is why a slower macroscopic cooling process ends up with worse flux expulsion. This is, of course, only a hypothesis and would need more experimental and theoretical evidence to back it up, so for now this question is still unanswered. Despite this, it is also clear that different values of u_0 have large effects on the amount of magnetic flux

which occurs in a superconductor, so it may also be valuable to explore making SRF cavities out of a material which has a different u_0 than Nb or Nb_3Sn.

4.2 Future Work

There are nearly unlimited degrees of freedom in these simulations, especially with this new material specific formulation we have derived for this project. It would not be hard to aimlessly and endlessly tweak parameters, but there are a few simulations which can be investigated with the current code that we suggest for future projects. Firstly, more simulations could be run to investigate this 'smearing' hypothesis we made at the end of Section 4.1. These simulations could involve using steeper and less steep triangle waves to get more or less gradual slopes in $|\psi|^2$, or they could also involve using different periodic functions which do not just have a single linear slope. It may also be interesting to orient our temperature gradient in the y direction so that we can try different gradient magnitudes and forms that don't necessarily have to be periodic. Additionally, we only looked at vortices interacting with a single pinning site at a time. A fuller understanding of the effect of pinning sites could be reached by running simulations with more pinning sites, perhaps randomly spreading them throughout the domain, and determining if there is some critical mass of pinning sites where vortices are no longer able to be pushed out without being pinned. Along these lines, simulations with multiple grain boundaries or even 'webs' of grain boundaries could give a clearer picture of how these defects behave when there is more than just a single grain boundary in either vertical or horizontal orientation. This thesis mostly focused on phenomena which occurred when temperature waves move very fast. It may be worth it to determine whether there are qualitative differences in very slow moving waves. For example, in Figure 3.13 there is a small bulge where the pinning site is, but it does not actually become a vortex, perhaps a very slow moving wave would allow a vortex more time to nucleate.

As for more major questions to investigate, there are a few natural places to go from this point. Firstly, while 2D simulations are useful for simulating important qualitative phenomena in superconductors, one of the main limitations is that defects are always parallel

with the magnetic field in 2D, whereas this is not necessarily the case in 3D [21]. As such, a natural extension of this project would be to investigate cooling and material defects in 3D. Additionally, in all of our simulations in this project we had full control over the temperature, but in reality, vortex movement can also dissipate some heat which would affect the temperature, so a future extension of our formulation may be to couple it to the heat diffusion equation to allow for these effects on our solutions. Finally, another extension which could be made to our simulations would be to allow portions of our domain to not be superconductors at all, with which we could simulate a small vacuum between grains or the interface between the surface of the superconductor and the space outside it. We would need to solve the Maxwell equations rather than the TDGL equations in these non-superconductor regions and enforce the appropriate boundary conditions. Overall, there are a lot of interesting remaining questions yet to be answered in this promising area of research.

Appendix A

Nondimensionalizing the Ginzburg-Landau Equations

A.1 Initial Equations and Useful Values

We will first nondimensionalize the time independent Ginzburg-Landau equations, listed below (it should be noted that Appendix A is closely related to work done in [11] and [17]):

$$\frac{1}{2m_s}\left(-i\hbar\nabla - \frac{e_s}{c}\mathbf{A}\right)^2\psi + \alpha\psi + \beta|\psi|^2\psi = 0 \text{ in the domain,} \tag{A.1.1}$$

$$\nabla\times\nabla\times\mathbf{A} - \frac{2\pi i e_s\hbar}{m_s c}\left(\psi^*\nabla\psi - \psi\nabla\psi^*\right) - \frac{4\pi e_s^2}{m_s c^2}|\psi|^2\mathbf{A} = 0 \text{ in the domain,} \tag{A.1.2}$$

$$\left(i\hbar\nabla\psi + \frac{e_s}{c}\mathbf{A}\psi\right)\cdot n = 0 \text{ on the boundary,} \tag{A.1.3}$$

$$\text{and } (\nabla\times\mathbf{A})\times n = \mathbf{H}\times n \text{ on the boundary.} \tag{A.1.4}$$

To nondimensionalize these equations, we first start by getting a few useful constants from these equations. The coherence length, ξ, can be found by looking at equation A.1.1, and letting $\mathbf{A} = 0$,

$$\nabla^2\psi + \frac{1}{\xi^2}\left(\psi + \frac{\beta}{\alpha}\psi^3\right) = 0, \tag{A.1.5}$$

where $\xi^2 = \frac{-\hbar^2}{2m_s\alpha}$. The coherence length is the length scale for the variance of ψ. The penetration depth, λ, can be found by looking at equation A.1.2 and considering the material to be perfectly superconducting, i.e. $\psi = \psi_0 = \left(\frac{-\alpha}{\beta}\right)^{\frac{1}{2}}$, this makes the second term in the equation go to 0 and we get

$$\nabla\times\nabla\times\mathbf{A} + \frac{1}{\lambda^2}\mathbf{A} = 0, \tag{A.1.6}$$

where $\lambda^2 = \frac{m_s c^2}{4\pi e_s^2 |\psi_0|^2} = \frac{-\beta m_s c^2}{4\pi e_s^2 \alpha}$. The penetration depth is a length scale for how deep magnetic field is able to penetrate into a superconducting material. We now have the well known Ginzburg-Landau parameter, $\kappa = \frac{\lambda}{\xi} = \sqrt{\frac{\beta}{2\pi}} \frac{m_s c}{e_s \hbar}$. The material's critical field, $H_c = \frac{4\pi\alpha^2}{\beta}$, also becomes a useful constant later.

A.2 Nondimensionalization

To nondimensionalize the GL equations, we make a number of coordinate transformations: $x = \lambda x'$ (and therefore $\nabla = \frac{1}{\lambda}\nabla'$), $\mathbf{A} = \sqrt{2} H_c \lambda \mathbf{A}'$, and $\psi = \sqrt{\frac{-\alpha}{\beta}}\psi'$. Doing this to equation A.1.1 yeilds

$$\frac{1}{2m_s}\left(\frac{-i\hbar}{\lambda}\nabla' - \frac{\sqrt{2}H_c\lambda e_s}{c}\mathbf{A}'\right)^2 \sqrt{\frac{-\alpha}{\beta}}\psi' + \alpha\sqrt{\frac{-\alpha}{\beta}}\psi' + \beta\sqrt{\frac{-\alpha}{\beta}}^3 |\psi'|^2\psi' = 0. \tag{A.2.1}$$

Dropping the primes and dividing by $\alpha\sqrt{\frac{-\alpha}{\beta}}$ results in

$$\frac{1}{2m_s\alpha}\left(\frac{-i\hbar}{\lambda}\nabla - \frac{\sqrt{2}H_c\lambda e_s}{c}\mathbf{A}\right)^2 \psi + \psi - |\psi|^2\psi = 0. \tag{A.2.2}$$

If we bring the $\frac{1}{2m_s\alpha}$ into the parentheses of the first term (square rooting it of course), and expand out the λs and Hc, you will see that the term in front of $\mathbf{A}$ goes to 1, and the term in front of the ∇ goes to $\frac{-i}{\kappa}$, so the final equation is

$$\left(\frac{-i}{\kappa}\nabla - \mathbf{A}\right)^2 \psi + \psi - |\psi|^2\psi = 0. \tag{A.2.3}$$

If we make the same transformations for equation A.1.2, we get

$$\frac{\sqrt{2}H_c}{\lambda}\nabla\times\nabla\times\mathbf{A}' + \frac{2\pi i e_s\hbar\alpha}{m_s c\lambda\beta}\left(\psi\prime^*\nabla'\psi' - \psi'\nabla'\psi\prime^*\right) + \frac{4\pi e_s^2\alpha}{m_s c^2\beta}|\psi'|^2\sqrt{2}H_c\lambda\mathbf{A}' = 0. \tag{A.2.4}$$

Once again dropping the primes and then multiplying by $\frac{\lambda}{\sqrt{2}H_c}$ gives

$$\nabla\times\nabla\times\mathbf{A} + \frac{2\pi i e_s\hbar\alpha}{m_s c\sqrt{2}H_c\beta}\left(\psi^*\nabla\psi - \psi\nabla\psi^*\right) + \frac{4\pi e_s^2\alpha\lambda^2}{m_s c^2\beta}|\psi|^2\mathbf{A} = 0. \tag{A.2.5}$$

Expanding H_c and λ again makes the coefficients in front of the second term reduce to $\frac{i}{2\kappa}$, and the terms in front of $|\psi|^2\mathbf{A}$ reduce to 1 so we get

$$\nabla\times\nabla\times\mathbf{A} + \frac{i}{2\kappa}\left(\psi^*\nabla\psi - \psi\nabla\psi^*\right) + |\psi|^2\mathbf{A} = 0. \tag{A.2.6}$$

For the first boundary condition, it follows the same process as for the first term in equation A.2.3, and doing the transformations for the last boundary equation, there will be $\sqrt{2}Hc$ in front of both terms, which cancel, so the final nondimensionalized equations are

$$\left(\frac{-i}{\kappa}\nabla - \mathbf{A}\right)^2 \psi + \psi - |\psi|^2\psi = 0, \tag{A.2.7}$$

$$\nabla \times \nabla \times \mathbf{A} + \frac{i}{2\kappa}\left(\psi^*\nabla\psi - \psi\nabla\psi^*\right) + |\psi|^2\mathbf{A} = 0, \tag{A.2.8}$$

$$\left(\frac{i}{\kappa}\nabla\psi + \mathbf{A}\psi\right)\cdot n = 0, \tag{A.2.9}$$

$$\text{and } (\nabla \times \mathbf{A}) \times n = \mathbf{H} \times n. \tag{A.2.10}$$

A.3 α and β Spacial Dependence

Now we want to let α and β vary with space, this can represent different materials, or material defects. To do this, we make the transformations $\alpha = \alpha_0 a(\mathbf{r})$ and $\beta = \beta_0 b(\mathbf{r})$, where α_0 and β_0 are constant reference values with the same units as α and β, and a and b are dimentionless functions of position. Returning to our definitions of ξ and λ, we see that setting $\mathbf{A} = 0$ in equation A.1.1 and collecting terms gives

$$\nabla^2\psi + \frac{1}{\xi_0^2}\left(a\psi + \frac{\beta_0}{\alpha_0}b\psi^3\right) = 0. \tag{A.3.1}$$

Where $\xi_0^2 = \frac{-\hbar^2}{2m_s\alpha_0}$. To find the other length scale we once again let the material be perfectly superconducting, but this time in terms of the reference α and β; $\psi = \psi_0 = \left(\frac{-\alpha_0}{\beta_0}\right)^{\frac{1}{2}}$, this makes equation A.1.2 become

$$\nabla \times \nabla \times \mathbf{A} + \frac{1}{\lambda_0^2}\mathbf{A} = 0, \tag{A.3.2}$$

where $\lambda_0^2 = \frac{m_s c^2}{4\pi e_s^2|\psi_0|^2} = \frac{-\beta_0 m_s c^2}{4\pi e_s^2 \alpha_0}$. Similarly, H_c becomes $H_{c0} = \frac{4\pi\alpha_0^2}{\beta_0}$, and $\kappa_0 = \frac{\lambda_0}{\xi_0} = \sqrt{\frac{\beta_0}{2\pi}}\frac{m_s c}{e_s\hbar}$. We then do the same process as we did before, but replacing any λ, ξ, κ, or H_c with λ_0, ξ_0, κ_0, or H_{c0}. This will result in almost the same equations, but with an a and a b in front of

the ψ and $|\psi|^2\psi$ terms:

$$\left(\frac{-i}{\kappa_0}\nabla - \mathbf{A}\right)^2 \psi + a\psi - b|\psi|^2\psi = 0, \tag{A.3.3}$$

$$\nabla \times \nabla \times \mathbf{A} + \frac{i}{2\kappa_0}\left(\psi^*\nabla\psi - \psi\nabla\psi^*\right) + |\psi|^2\mathbf{A} = 0, \tag{A.3.4}$$

$$\left(\frac{i}{\kappa_0}\nabla\psi + \mathbf{A}\psi\right)\cdot n = 0, \tag{A.3.5}$$

$$\text{and } (\nabla \times \mathbf{A}) \times n = \mathbf{H} \times n. \tag{A.3.6}$$

A.4 Time Dependent Ginzburg-Landau Equations

The Time Dependent Ginzburg-Landau equations are

$$\frac{1}{2m_s}\left(-i\hbar\nabla - \frac{e_s}{c}\mathbf{A}\right)^2\psi + \alpha\psi + \beta|\psi|^2\psi + \Gamma\left(\frac{\partial\psi}{\partial t} + \frac{ie_s\theta}{\hbar}\psi\right) = 0 \text{ in the domain,} \tag{A.4.1}$$

$$\nabla\times\nabla\times\mathbf{A} - \frac{2\pi i e_s\hbar}{m_s c}\left(\psi^*\nabla\psi - \psi\nabla\psi^*\right) - \frac{4\pi e_s^2}{m_s c^2}|\psi|^2\mathbf{A} + \frac{4\pi\sigma_n}{c}\left(\frac{1}{c}\frac{\partial\mathbf{A}}{\partial t} + \nabla\theta\right) = 0 \text{ in the domain,} \tag{A.4.2}$$

$$\left(i\hbar\nabla\psi + \frac{e_s}{c}\mathbf{A}\psi\right)\cdot n = 0 \text{ on the boundary,} \tag{A.4.3}$$

$$(\nabla \times \mathbf{A}) \times n = \mathbf{H} \times n \text{ on the boundary,} \tag{A.4.4}$$

$$\text{and } -\left(\nabla\theta + \frac{\partial\mathbf{A}}{\partial t}\right)\cdot n = 0 \text{ on the boundary.} \tag{A.4.5}$$

We will start with α and β constant in time and space. To nondimensionalize these equations, we first use the same definitions for λ, ξ, κ, and H_c as we defined in section A.1. We also make the same change of variables as in section A.2 in addition to letting $t = \tau_\Delta t'$ and $\theta = \kappa\theta_0\theta'$; For equation A.4.1, this gives us

$$\begin{aligned}\frac{1}{2m_s}\left(\frac{-i\hbar}{\lambda}\nabla' - \frac{\sqrt{2}H_c\lambda e_s}{c}\mathbf{A}'\right)^2\sqrt{\frac{-\alpha}{\beta}}\psi' + \alpha\sqrt{\frac{-\alpha}{\beta}}\psi' + \beta\sqrt{\frac{-\alpha}{\beta}}^3|\psi'|^2\psi' \\ +\Gamma\sqrt{\frac{-\alpha}{\beta}}\left(\frac{1}{\tau_\Delta}\frac{\partial\psi'}{\partial t'} + \frac{ie_s\kappa\theta_0\theta'}{\hbar}\psi'\right) = 0,\end{aligned} \tag{A.4.6}$$

and dropping the primes and dividing by $\alpha\sqrt{\frac{-\alpha}{\beta}}$ gives

$$\frac{1}{2m_s\alpha}\left(\frac{-i\hbar}{\lambda}\nabla - \frac{\sqrt{2}H_c\lambda e_s}{c}\mathbf{A}\right)^2\psi + \psi - |\psi|^2\psi + \frac{\Gamma}{|\alpha|}\left(\frac{1}{\tau_\Delta}\frac{\partial\psi}{\partial t} + \frac{ie_s\kappa\theta_0\theta}{\hbar}\psi\right) = 0. \tag{A.4.7}$$

The first three terms reduce down to the same terms as in equation A.2.7. We then let $\tau_\Delta = \frac{\Gamma}{|\alpha|}$ and $\theta_0 = \frac{\hbar}{e_s \tau_\Delta}$ to get the final equation:

$$\left(\frac{-i}{\kappa}\nabla - \mathbf{A}\right)^2 \psi + \psi - |\psi|^2\psi + \frac{\partial \psi}{\partial t} + i\kappa\theta\psi = 0. \tag{A.4.8}$$

Making the same coordinate transformations for equation A.4.2 we get

$$\begin{aligned}\frac{\sqrt{2}H_c}{\lambda}\nabla\times\nabla\times\mathbf{A}' + \frac{2\pi i e_s \hbar\alpha}{m_s c\lambda\beta}\left(\psi'^*\nabla'\psi' - \psi'\nabla'\psi'^*\right) + \frac{4\pi e_s^2\alpha}{m_s c^2\beta}|\psi'|^2\sqrt{2}H_c\lambda\mathbf{A}' \\ + \frac{4\pi\sigma_n}{c}\left(\frac{\sqrt{2}H_c\lambda}{c\tau_\Delta}\frac{\partial\mathbf{A}'}{\partial t'} + \frac{\kappa\theta_0}{\lambda}\nabla'\theta'\right) = 0,\end{aligned} \tag{A.4.9}$$

and dropping the primes and then multiplying by $\frac{\lambda}{\sqrt{2}H_c}$ gives

$$\nabla\times\nabla\times\mathbf{A} + \frac{2\pi i e_s\hbar\alpha}{m_s c\sqrt{2}H_c\beta}\left(\psi^*\nabla\psi - \psi\nabla\psi^*\right) + \frac{4\pi e_s^2\alpha\lambda^2}{m_s c^2\beta}|\psi|^2\mathbf{A} + \frac{4\pi\sigma_n}{c}\left(\frac{\lambda^2}{c\tau_\Delta}\frac{\partial\mathbf{A}}{\partial t} + \frac{\kappa\theta_0}{\sqrt{2}H_c}\nabla\theta\right) = 0. \tag{A.4.10}$$

Once again the first 3 terms go the the same as equation A.2.8. We then define $\tau_j = \frac{\sigma_n\beta m_s}{e_s^2|\alpha|}$, which gives

$$\nabla\times\nabla\times\mathbf{A} + \frac{i}{2\kappa}\left(\psi^*\nabla\psi - \psi\nabla\psi^*\right) + |\psi|^2\mathbf{A} + \frac{\tau_j}{\tau_\Delta}\frac{\partial\mathbf{A}}{\partial t} + \frac{4\pi\sigma_n\kappa\theta_0}{\sqrt{2}H_c c}\nabla\theta = 0. \tag{A.4.11}$$

If we define $u = \frac{\tau_\Delta}{\tau_j}$, then the coefficents in front of the time derivative go to $\frac{1}{u}$, and it turns out that if we substitute in the value for θ_0 we found earlier, the coefficients in front of the $\nabla\theta$ also go to $\frac{1}{u}$ and we get

$$\nabla\times\nabla\times\mathbf{A} + \frac{i}{2\kappa}\left(\psi^*\nabla\psi - \psi\nabla\psi^*\right) + |\psi|^2\mathbf{A} + \frac{1}{u}\left(\frac{\partial\mathbf{A}}{\partial t} + \nabla\theta\right) = 0. \tag{A.4.12}$$

Thus, the final equations are

$$\left(\frac{-i}{\kappa}\nabla - \mathbf{A}\right)^2 \psi + \psi - |\psi|^2\psi + \frac{\partial\psi}{\partial t} + i\kappa\theta\psi = 0, \tag{A.4.13}$$

$$\nabla\times\nabla\times\mathbf{A} + \frac{i}{2\kappa}\left(\psi^*\nabla\psi - \psi\nabla\psi^*\right) + |\psi|^2\mathbf{A} + \frac{1}{u}\left(\frac{\partial\mathbf{A}}{\partial t} + \nabla\theta\right) = 0, \tag{A.4.14}$$

$$\left(\frac{i}{\kappa}\nabla\psi + \mathbf{A}\psi\right)\cdot n = 0 \tag{A.4.15}$$

$$(\nabla\times\mathbf{A})\times n = \mathbf{H}\times n, \tag{A.4.16}$$

$$\text{and } -\left(\nabla\theta + \frac{\partial\mathbf{A}}{\partial t}\right)\cdot n = 0. \tag{A.4.17}$$

A.5 α, β, and Γ vary with time and space

If we now let $\alpha = \alpha_0 a(\mathbf{r},t)$, $\beta = \beta_0 b(\mathbf{r},t)$, and $\Gamma = \Gamma_0\gamma(\mathbf{r},t)$, we can do the same thing as we did in section A.3, and let $\xi_0^2 = \frac{-\hbar^2}{2m_s\alpha_0}$, $\lambda_0^2 = \frac{m_s c^2}{4\pi e_s^2|\psi_0|^2} = \frac{-\beta_0 m_s c^2}{4\pi e_s^2\alpha_0}$, $H_{c0} = \frac{4\pi\alpha_0^2}{\beta_0}$, and $\kappa_0 = \frac{\lambda_0}{\xi_0} = \sqrt{\frac{\beta_0}{2\pi}}\frac{m_s c}{e_s\hbar}$. Additionally we also let $\tau_{\Delta 0} = \frac{\Gamma_0}{|\alpha_0|}$, $\tau_{j0} = \frac{\sigma_n\beta_0 m_s}{e_s^2|\alpha_0|}$, $u_0 = \frac{\tau_{\Delta 0}}{\tau_{j0}}$, and $\theta_0 = \frac{\hbar}{e_s\tau_{\Delta 0}}$. We can then follow the same steps as above with these new values and we get

$$\left(\frac{-i}{\kappa_0}\nabla - \mathbf{A}\right)^2\psi + a\psi - b|\psi|^2\psi + \gamma\left(\frac{\partial\psi}{\partial t} + i\kappa_0\theta\psi\right) = 0, \tag{A.5.1}$$

$$\nabla\times\nabla\times\mathbf{A} + \frac{i}{2\kappa_0}\left(\psi^*\nabla\psi - \psi\nabla\psi^*\right) + |\psi|^2\mathbf{A} + \frac{1}{u_0}\left(\frac{\partial\mathbf{A}}{\partial t} + \nabla\theta\right) = 0, \tag{A.5.2}$$

$$\left(\frac{i}{\kappa_0}\nabla\psi + \mathbf{A}\psi\right)\cdot n = 0 \tag{A.5.3}$$

$$(\nabla\times\mathbf{A})\times n = \mathbf{H}\times n, \tag{A.5.4}$$

$$\text{and } -\left(\nabla\theta + \frac{\partial\mathbf{A}}{\partial t}\right)\cdot n = 0. \tag{A.5.5}$$

Bibliography

[1] Margaret Sunde et al. "Common core structure of amyloid fibrils by synchrotron X-ray diffraction 1 1Edited by F. E. Cohen". In: *Journal of Molecular Biology* 273.3 (1997), pp. 729–739. DOI: 10.1006/jmbi.1997.1348.

[2] Chu [Ryang Wie]. "High resolution x-ray diffraction characterization of semiconductor structures". In: *Materials Science and Engineering: R: Reports* 13.1 (1994), pp. 1–56. ISSN: 0927-796X. DOI: https://doi.org/10.1016/0927-796X(94)90008-6. URL: http://www.sciencedirect.com/science/article/pii/0927796X94900086.

[3] J.B. Kortright et al. "Research frontiers in magnetic materials at soft X-ray synchrotron radiation facilities". In: *Journal of Magnetism and Magnetic Materials* 207.1 (1999), pp. 7–44. ISSN: 0304-8853. DOI: https://doi.org/10.1016/S0304-8853(99)00485-0. URL: http://www.sciencedirect.com/science/article/pii/S0304885399004850.

[4] Andrew Robert. Steere. "A Timeline of Major Particle Accelerators". MA thesis. 2005.

[5] H Padamsee, K W Shepard, and R Sundelin. "Physics and Accelerator Applications of RF Superconductivity". In: *Annual Review of Nuclear and Particle Science* 43.1 (1993), pp. 635–686. DOI: 10.1146/annurev.ns.43.120193.003223.

[6] Samuel Elliott. Posen and Matthias Ulf Liepe. "Understanding and Overcoming Limitation Mechanisms in Nb3Sn Superconducting RF Cavities". PhD thesis. 2015.

[7] Alden Pack. "Computational Exploration of Vortex Nucleation in Type II Superconductors Using a Finite Element Method in Ginzburg-Landau Theory". MA thesis. 2017.

[8] Dirk Van Delft and Peter Kes. "The discovery of superconductivity". In: *Physics Today* 63.9 (2010), pp. 38–43.

[9] Michael Tinkham. *Superconductivity*. Gordon and Breach, 1966.

[10] S Jonathan Chapman, Sam D Howison, and John R Ockendon. "Macroscopic models for superconductivity". In: *Siam Review* 34.4 (1992), pp. 529–560.

[11] Qiang Du, Max D. Gunzburger, and Janet S. Peterson. "Analysis and Approximation of the Ginzburg–Landau Model of Superconductivity". In: *SIAM Review* 34.1 (1992), pp. 54–81. DOI: 10.1137/1034003.

[12] Sam Posen and Matthias Liepe. "Advances in development of Nb 3 Sn superconducting radio-frequency cavities". In: *Physical Review Special Topics-Accelerators and Beams* 17.11 (2014), p. 112001.

[13] S. Posen et al. "Efficient expulsion of magnetic flux in superconducting radiofrequency cavities for high Q0 applications". In: *Journal of Applied Physics* 119.21 (2016), p. 213903. DOI: 10.1063/1.4953087.

[14] Hans Petter Langtangen and Anders Logg. *Solving PDEs in Python*. Springer, 2017. ISBN: 978-3-319-52461-0. DOI: 10.1007/978-3-319-52462-7.

[15] Huadong Gao. "Efficient Numerical Solution of Dynamical Ginzburg-Landau Equations under the Lorentz Gauge". In: *Communications in Computational Physics* 22.1 (2017), pp. 182–201. DOI: 10.4208/cicp.OA-2016-0120.

[16] Huadong Gao and Weiwei Sun. "An efficient fully linearized semi-implicit Galerkin-mixed FEM for the dynamical Ginzburg–Landau equations of superconductivity". In: *Journal of Computational Physics* 294 (2015), pp. 329–345. DOI: 10.1016/j.jcp.2015.03.057.

[17] N. B. Kopnin. *Theory of nonequilibrium superconductivity*. Oxford University Press, 2009.

[18] Bakhrom Oripov and Steven Anlage. "Time-dependent Ginzburg-Landau treatment of rf magnetic vortices in superconductors: Vortex semiloops in a spatially nonuniform magnetic field". In: *Physical Review E* 101 (Mar. 2020). DOI: 10.1103/PhysRevE.101.033306.

[19] Ricardo Vega Monroy, J. Castillo, and D. Torres. "Vortex Dynamics Equation in Type-II Superconductors in a Temperature Gradient". In: *Brazilian Journal of Physics - BRAZ J PHYS* 40 (Dec. 2010), pp. 443–449. DOI: 10.1590/S0103-97332010000400015.

[20] Jared Carlson et al. "Analysis of Magnetic Vortex Dissipation in Sn-Segregated Boundaries in Nb_3Sn SRF Cavities". In: *arXiv e-prints*, arXiv:2003.03362 (Mar. 2020), arXiv:2003.03362. arXiv: 2003.03362 [cond-mat.supr-con].

[21] Alden R. Pack et al. "Role of surface defects and material inhomogeneities for vortex nucleation in superconductors within time-dependent Ginzburg-Landau theory in 2 and 3 dimensions". In: *arXiv e-prints*, arXiv:1911.02132 (Nov. 2019), arXiv:1911.02132. arXiv: 1911.02132 [physics.comp-ph].

[22] Qiang Du. "Finite element methods for the time-dependent Ginzburg-Landau model of superconductivity". In: *Computers & Mathematics with Applications* 27.12 (1994), pp. 119–133. DOI: 10.1016/0898-1221(94)90091-4.

[23] S. Posen et al. "Role of magnetic flux expulsion to reach $Q_0 > 3 \times 10^{10}$ in superconducting rf cryomodules". In: *Phys. Rev. Accel. Beams* 22 (3 Mar. 2019), p. 032001. DOI: 10.1103/PhysRevAccelBeams.22.032001. URL: https://link.aps.org/doi/10.1103/PhysRevAccelBeams.22.032001.